Atmos. Chem. Phys. Discuss., 9, 26777–26832, 2009
www.atmos-chem-phys-discuss.net/9/26777/2009/

Atmospheric Chemistry and Physics Discussions

This discussion paper is/has been under review for the journal Atmospheric Chemistry and Physics (ACP). Please refer to the corresponding final paper in ACP if available.

Cirrus cloud radiative effect on surface-level shortwave and longwave irradiances at regional and global scale

J.-C. Dupont[1], **M. Haeffelin**[1], **and C. N. Long**[2]

[1]Institut Pierre et Simon Laplace, Ecole Polytechnique, Palaiseau, France
[2]Pacific Northwest National Laboratory, Richland, WA, USA

Received: 2 November 2009 – Accepted: 1 December 2009 – Published: 15 December 2009

Correspondence to: J.-C. Dupont (jean-charles.dupont@ipsl.polytechnique.fr)

Published by Copernicus Publications on behalf of the European Geosciences Union.

Abstract

Data collected at four ground-level sites are analyzed (1) to determine the surface cloud radiative effect (CRE) induced by cirrus clouds at regional scale for shortwave (CRE_{SW}) and longwave (CRE_{LW}) fluxes and (2) to derive the sensitivity of surface CRE_{SW} to the cloud optical thickness (COT) modulated by the solar zenith angle and the atmospheric turbidity (noted $CRE_{SW}*$) and the sensitivity of surface CRE_{LW} to the infrared emissive power of cirrus cloud modulated by the water vapor content (noted $CRE_{LW}*$). The average $CRE_{SW}*$ is $-120\,W\,m^{-2}\,COT^{-1}$ but it ranges from -80 to $-140\,m^{-2}\,COT^{-1}$ depending on the solar illumination with a residual variability ranges from $+40$ and $-40\,W\,m^{-2}\,COT^{-1}$ from pristine to turbid conditions, respectively. The $CRE_{LW}*$, that corresponds to the infrared transmissivity of the atmosphere, ranges from 3% to 40% from dry to wet atmospheric conditions, respectively. The subvisible cirrus class (COT<0.03) over mid-latitude sites, that represents 20% of the population, induces a significant increase in surface LW irradiance at the 2–7 $W\,m^{-2}$ level. The semi-transparent cirrus class (0.03<COT<0.3), that represents 45% of the population, will affect the surface SW irradiance by -12 to $-25\,W\,m^{-2}$. Cloud-Aerosol Lidar and Infrared Pathfinder Satellite Observations (CALIPSO) and the Atmospheric Infrared Sounder (AIRS) are used here to estimate the surface radiative effect at global scale. Global CRE estimations show very significant zonal and seasonal variability of each component of the CRE_{NET}. CRE_{NET} is $0.4\,W\,m^{-2}$ during winter/autumn for 15–75° N and $1\,W\,m^{-2}$ for 45–75° S whereas it is near $-3\,W\,m^{-2}$ for 15° S–15° N. The summer period shows a cirrus cloud global cooling at all the latitudes except for 75–45° S with a quasi null effect and a peak at $-3.6\,W\,m^{-2}$ for 15° S–45° N. The global average cumulative CRE is -2.8, 1.7 and $-1.1\,W\,m^{-2}$ for CRE_{SW}, CRE_{LW}, and CRE_{NET}, respectively.

ACPD

9, 26777–26832, 2009

1 Introduction

Clouds at all levels of the atmosphere play a significant role in the energy budget of the Earth-atmosphere system by their effects on the transfer of radiant energy through the atmosphere by their competing greenhouse and albedo effects (Hansen et al., 1997). They are one of the largest sources of uncertainty in predicting potential future climate change (Wielicki et al., 1995; Houghton et al., 2001). The cloud radiative effect (CRE) defined as the difference between all-sky and clear-sky radiative fluxes is a simple but effective means of studying cloud-radiation interactions and diagnosing problems in general circulation models (Cess et al., 1990). Proper partitioning of the cloud radiative impact between the surface and the top of atmosphere (TOA) is essential for assessing and modeling the effects of clouds on climate.

Numerous studies have demonstrated that the global average frequency of cirrus cloud occurrence is near 17% (Dessler et al., 2003; Sassen et al., 2008) and can reach 45% in the tropics (Stubenrauch et al., 2006) with a maximum occurrence frequency up to 70% near the tropics over the 100–180° E longitude band (Nazaryan et al., 2008). The significant coverage of cirrus clouds, their persistence, their large area extent, and their high altitude make them important components in the total radiation budget and in the vertical transport of energy through radiative processes (Stephens, 2005). Since Liou (1986) these clouds have been identified as one of the sources of uncertainty in the study of Earth's radiation budget and climate.

In the last few decades our knowledge on the effect of cirrus clouds on TOA has been improved substantially with the long time series of shortwave (SW) and longwave (LW) TOA irradiances available from the Earth Radiation Budget Experiment (ERBE; Barkstrom, 1986), from Clouds and the Earth's Radiant Energy System (CERES; Wielicki et al., 1998) or from the Geostationary Earth Radiation Budget (GERB; Harries et al., 2005). Satellites derived TOA CRE and yielded a CRE_{SW} (CRE_{LW}) ranging from −20 to −350 $W\,m^{-2}$ (5 to 200 $W\,m^{-2}$) depending on cloud type and cloud cover (Chen et

ACPD
9, 26777–26832, 2009

al., 2000; Choi et al., 2006; Stubenrauch et al., 2006). Despite the opposite signs of CRE_{LW} and CRE_{SW}, CRE_{NET} (CRE_{NET}=CRE_{SW}+CRE_{LW}) at the TOA has positive values for cirrus clouds ranging from 1.0/1.6 $W m^{-2}$ near the tropics (Haladay and Stephens, 2009; Lee et al., 2009) to 5.4 $W m^{-2}$ in global average (Chen et al., 2000) and negative values for thick clouds reaching −80 $W m^{-2}$ for low level stratiform clouds in the middle latitude (Ramanathan et al., 1989; Chen et al., 2000).

Cirrus cloud radiative effect at the surface can be estimated by using empirical parameterizations derived from radiative transfer model calculations applied to satellites observations. However, satellite-derived CRE and ground-based measured CRE are generally in good agreement, but a residual difference near 50 $W m^{-2}$ appears in the older data sets (Li and Leighton, 1993) due to difficulties in the modeling of the cloudy-sky SW radiation (Cess et al., 1995). Ackerman et al. (2003) managed to reduce the discrepancies to less than 10% and Chen et al. (2000) find that on global average, the effect of a cirrus cloud on surface irradiances is +8 $W m^{-2}$ for CRE_{LW} and −22 $W m^{-2}$ for CRE_{SW}. Moreover, Chen et al. (2000) show that cloud types with larger areal extents may have stronger effects on the Earth radiation budget and conclude that cirrus and stratus clouds result in similar cumulative effects. In the tropics, Lee et al. (2009) and Haladay and Stephens (2009) show a net cooling effect at the surface of −1.35 $W m^{-2}$ and −1 $W m^{-2}$, respectively.

However, the possible contamination of clear-sky pixels by thin cirrus composed of complex shape particles complicate the scattering and absorption of radiation and modeling of radiative transfer through these clouds (Lo et al., 2006). Satellite observations of thin cirrus also have emerged over the last several years. Infrared vertical sounders such as the TIROS-N Operational Vertical Sounder (TOVS; Stubenrauch et al., 1999) have been used to examine the seasonal variability of thin cirrus properties (Stubenrauch et al., 2006) and trends in thin clouds (Wylie and Menzel, 1999), but only for clouds with a optical thickness greater than 0.2. Active optical sensors, such as Cloud-Aerosol Lidar with Orthogonal Polarization (CALIOP, Winker et al., 2009), are very sensitive to scattering by particles, with detection limits as low as 0.01 optical

ACPD
9, 26777–26832, 2009

thickness, which allows them to document the distribution of thin cirrus clouds and their vertical structure (Sassen et al., 2008) in much greater details.

To precisely quantify the surface CRE and to understand the relationship between the CRE and cloud/atmospheric properties, accurate measurements have to be taken of each parameter added simultaneously to radiation measurements. That is why, several surface sites like those operated by the US Department of Energy Atmospheric Radiation Measurement Program (ARM; Ackerman and Stokes, 2003) and by the Site Instrumental de Recherche par Télédétection Atmosphérique (SIRTA; Haeffelin et al., 2005) have been developed to explore surface CRE variability. Starting from these long-term period data sets, several studies have been conducted such as Mace et al. (2006) and Dong et al. (2005) over the Southern Great Plains (SGP) site and Dupont and Haeffelin (2008) over the SIRTA site. Mace et al. (2006) show that the predominant surface CREs are associated with thin cirrus cloud layers and thick low-level clouds, due in part to their very frequent occurrence compared to other types of clouds. Dong et al. (2005) establish correlations between cloud fraction and surface CRE and quantify the seasonal cycle of CRE showing an average annual CRE_{SW} (CRE_{LW}) of $-37\,W\,m^{-2}$ ($17\,W\,m^{-2}$) for high altitude clouds. Finally, Dupont and Haeffelin (2008) quantify the relationship between CRE and cirrus cloud and atmospheric properties. CRE_{SW} (CRE_{LW}) is driven by cloud optical thickness and atmospheric turbidity (water vapor amount and cirrus infrared emissive power).

In this paper, we present (1) the correlations between CRE and macrophysical and optical properties of cirrus cloud modulated by atmospheric compositions, (2) the monthly CRE_{SW} and CRE_{LW} cycle for continental, arctic, tropical, and oceanic sites and (3) the global distribution of surface CRE induced by cirrus cloud for 2006–2007 periods. In Sect. 1, we present the ground-based and spatial measurements used in this study and the methods to identify both clear-sky and persistent cirrus cloud situations. In Sect. 2, we establish two parametric relationships: one between CRE_{SW} and cloud optical thickness, solar zenith angle and atmospheric turbidity; and one between CRE_{LW} and the infrared emissive power of cirrus cloud and water vapor content.

ACPD
9, 26777–26832, 2009

Finally, Sect. 3 presents (1) the annual cycle of CRE_{SW} and CRE_{LW} for each ground-based site and (2) the instantaneous and cumulative cirrus cloud radiative effect at global scale starting from parameterizations developed in Sect. 2 and CALIOP/AIRS input data.

2 Observations data set

2.1 Ground-based measurement

To quantify the cirrus cloud radiative effect at the surface, the following measurements are required: (1) high quality downwelling shortwave and longwave irradiance measurements, (2) screen-level temperature and water-vapor pressure, (3) column-integrated water vapor density and aerosol optical thickness, (4) vertical profiles of temperature, and finally (5) unambiguous identification of cloud-free and cloudy situations.

We use measurements from two midlatitude sites, the SIRTA Observatory (Haeffelin et al., 2005) and the ARM SGP Lamont site (Ackerman and Stokes, 2003), the ARM Tropical Western Pacific Nauru site (Clements et al., 1999) and the ARM North Slope of Alaska Barrow site (Stamnes et al., 1998). Table 1 summarizes the instruments available at these four observatories that are used in this study. Routine radiation measurements are performed at SIRTA (ARM sites) using a CH1 (NIP) pyrheliometer, a shaded CM22 (PSP) pyranometer for the solar components, and a shaded CG4 (PIR) pyrgeometer for the longwave component. Integrated water vapor (IWV) measurements are provided by a microwave radiometer (ARM sites), or by GPS (Global Positionning System) receiver or by AERONET sunphotometer during cloud-free situations (SIRTA). Aerosol optical thickness is provided by AERONET sunphotometer network retrievals with automatic cloud screening (e.g., 2.0 products). Temperature, pressure, relative humidity, and wind profiles are obtained from radiosonde measurements performed over each site at 00:00 UT and 12:00 UT. Atmospheric column measurements

ACPD
9, 26777–26832, 2009

are complemented by screen-level measurements of wind speed and direction, temperature, pressure, humidity and precipitation. Vertical distributions of particles (clouds and aerosols) are documented either by backscatter depolarization lidar on routine mode over the TWP and NSA sites and semi-automatic mode over the SIRTA site Haeffelin et al., 2005), exclusively operating during day or by Raman lidar over the SGP site on routine mode since 1998 (Ackerman and Stokes, 2003). These lidars are used to unambiguously identify the presence of liquid or ice water from the surface to 15 km high. Lidar products are obtained with a resolution time of 1 min for the SIRTA site, 10 min for the SGP site, and 10 s for the Barrow and Nauru sites.

These four multi-latitude sites are characterized by differing climate regimes e.g., US continental for Lamont, French oceanic/suburban for SIRTA and coastal tropical and arctic for Nauru and Barrow, respectively. The variability in terms of aerosols, water vapor, and clouds is very large between each site and permits the study of the impact of a range of atmospheric and high altitude cloud properties on shortwave and longwave irradiances received at the surface.

Figure 1a and 1b show the monthly variability of geophysical variables like integrated water vapor (Fig. 1a) and aerosols optical thickness (Fig. 1b). Figure 1c and 1d present the cirrus cloud base height for each site and the cloud optical thickness associated with these cirrus clouds. Cloud optical thickness is derived here from a combined analysis between lidar and sun-photometer data (Dupont et al. 2008), see explanation in Sect. 3.1.3. Table 2a shows the seasonal and annual averages of integrated water vapor (IWV in cm) and aerosol optical thickness (AOT). Table 2b shows the cirrus cloud base altitude (CBH in km) and optical thickness (COT) at the SGP, TWP, NSA and SIRTA sites.

Midlatitude and arctic sites are characterized by a significant annual cycle of column water vapor: maximum integrated water vapor amount appears in summer and reaches 3.8, 2.2, and 1.4 cm for the SGP, SIRTA and NSA sites, respectively. The TWP site exhibits a relatively constant high value of IWV ranging from 4.8 to 5.7 cm. The SIRTA and NSA sites are the driest sites with annual values of IWV near 1.5 cm. Hence, these

ACPD
9, 26777–26832, 2009

four sites exhibit a large span of IWV ranging from 0.3 cm (NSA in April) to almost 6.5 cm (TWP in January).

Aerosol optical thickness corresponds here to the level 2.0 AERONET product when an automatic cloud screening is applied. For the two midlatitude sites, AOT is very similar and ranges from 0.06 (winter period) to 0.12 (summer period). This increase during the summer period is due to the more frequently anticyclone period where AOT increases until a precipitation event. Over the TWP and the NSA sites, the monthly variability is much more important, and AOT ranges from 0.17 (TWP in July) to 0.03 (NSA in October). This too important value of AOT seems to include cirrus cloud in the data set. In fact, over the TWP site the overcast cirrus cloud period appears frequently and consequently the dataset must be more polluted by a cirrus cloud event.

Monthly CBH ranges from 8.5 to 10 km over the SIRTA sites and from 9 to 11.5 km over the SGP site as a result of a thicker summer troposphere. Hence, the annual cycle is significant over the SGP site with a winter CBH of 9.3 km and a summer CBH of 10.9 km. The TWP site does not show a significant annual cycle with however to maximum peak (12.8 km in May and 13 km in October), those correspond to the more intensive convection. All the variability of the CBH range is obtained with the lowest cirrus cloud over the NSA site (annual average value of 8.1 km) to the highest cirrus cloud over TWP (annual average value of 12 km).

Cumulative cloud optical thickness (COT) distribution shows the relative homogeneity of the COT except for the NSA site. Cirrus clouds also are classified according to their cloud optical thickness ranges: subvisible (COT<0.03), semi-transparent (0.03<COT<0.3), and thick (0.3<COT<3.0) (Sassen et al., 2001). For the SIRTA, SGP and TWP sites, subvisible, semi-transparent and thick cirrus clouds represent 20%, 50%, and 30%, respectively. Nevertheless, for the NSA site, subvisible, semi-transparent and thick cirrus clouds represent 40%, 43% and 17%, respectively. Cirrus clouds are optically thinner over the NSA site because of the significant occurrence of very thin polar stratospheric clouds (Noel et al., 2008). We do not see a significant annual cycle for the cirrus cloud optical thickness.

ACPD
9, 26777–26832, 2009

2.2 Spatial observations data set

Cirrus cloud and aerosol properties at global scale are obtained here by using observations from the CALIOP spaceborne lidar, part of the CALIPSO mission (Winker et al., 2009). The CALIPSO satellite was launched in April 2006 and passes in the same track every 16 days (Currey et al., 2007). Official CALIOP Level 2 (version 2) data products are used in this study (Currey et al., 2007). We use one year of CALIOP data products in the July 2006–June 2008 period to sample all seasons uniformly. Both daytime and nighttime data are considered. CALIOP cloud optical thickness retrievals use both the lidar ratio (LR) statistical method and the transmittance method (TR) (Sassen and Comstock, 2001; Young et al., 2009). Multiple scattering effects are taken into account by a parameterization (Winker, 2003). Level 2 version 2 data products used in this study are the cloud optical thickness, the cirrus cloud temperature, and the aerosol optical thickness. These parameters have been evaluated and validated (Dupont et al., 2009).

Integrated water vapor content at global scale is collected from the observations provided by The Atmospheric Infrared Sounder (AIRS). The AIRS was launched on the Aqua research satellite, a major component of NASA's Earth Observing System, in May 2002 (Divakarla et al., 2006). From its sun synchronous polar orbit, crossing the equator southward at 01:30 and northward at 13:30 LT (local time), the AIRS system provides more than 300 000 all-weather soundings covering more than 90% of the globe every 24 h. The geophysical parameters have been produced since the beginning of 2003 – the first data were released to the public in mid-2003 (Aumann et al., 2003). The temperature and water vapor profiles have been validated for both land and ocean for a broad range of geographic conditions (Divakarla et al., 2006; Tobin et al., 2006). Integrated water vapor level 2 version 5 data products are used in this study.

Cirrus cloud and atmospheric composition at global scale are based on statistics using all observations collected during a given time period. From the point of view of a ground-based observatory, the region of study is defined as the area that is sampled

ACPD
9, 26777–26832, 2009

by the zenith-looking remote sensing instruments and the spatial representativeness of the sampled area. Zenith-looking lidars sample very small volumes, but the horizontal coherence of clouds in the 7–15 km altitude domain is large, because 50% of the cloud population extends horizontally more than 100 km. From the point of view of the space-borne lidar, the spatial domain is a compromise between a small enough area around the observatory to remain consistent with the ground-based statistics, and a large enough area to obtain enough samples to derive statistics. Here we consider a domain to 2.5°×2.5° latitude-longitude box for CALIOP and AIRS data centered on each ground-level site.

2.3 Clear-sky and overcast period detection

In this study, the term "clear-sky" is defined as a sky without any liquid water or ice cloud. This definition differs from the standard one typically associated with human observations, and sky-imager and irradiance-based methodologies, which traditionally allow some amount of condensed water in the column to be classified as "clear-sky" (Dupont et al., 2008). Clear-sky periods during daytime are selected by two automated methods developed by Long and Ackerman (2000) and Dürr and Philipona (2004), respectively based on shortwave and longwave irradiances. However, the methodology developed by Long et al. (2006) for estimating fractional sky cover for an effective 160° field-of-view from an analysis of surface measurements of downwelling total and diffuse shortwave (SW) irradiance can be biased by optically-thin clouds (Dupont et al., 2008). Additionally, broadband downwelling longwave irradiances are known to be insensitive to the influence of high, cold clouds due to the emission from the intervening atmosphere. Hence, to be sure of the totally clear-sky (i.e., condensation-free) conditions, we add a threshold algorithm based on lidar measurements (Morille et al., 2007). Lidar backscatter measurements allow us to detect clouds with optical depth as low as about 0.005. Using these methods, 27, 51, 21, and 17 days with totally clear-sky conditions longer than 4 h are found for the SIRTA, SGP, TWP, and NSA sites, respectively. The average clear-sky period per day for these sites is 5.7, 4.3, 6.9, and 7.4 h, respectively.

ACPD
9, 26777–26832, 2009

An overcast period is defined as a minimum of 3 h period containing cirrus clouds (i.e., 180 profiles per hour for the SIRTA site, 18 profiles for the SGP site, and 1080 profiles for the TWP and NSA sites). This ensures homogenous radiative fields. Only clouds with base altitude higher than 7 km are considered here with no cloud below for the SGP, SIRTA and TWP site. Concerning the NSA site, we consider all clouds higher than 4 km in order not to consider only Polar Stratospheric Clouds characterized by particular microphysical and optical properties (Noel et al., 2008). Additionally, only overcast periods longer than 3 h are considered to ensure a persistent impact on LW and SW irradiances. When an overcast period exceeding 3 h is detected, we consider every 15 min samples to process the cirrus cloud radiative effect. Based on these criteria, we identify 73, 83, 80, and 21 days with totally overcast conditions induced by high altitude clouds for the SIRTA, SGP, TWP and NSA sites, respectively, and what correspond to an average time per day for these overcast conditions of 4.8, 3.5, 4.3, and 3.2 h for each site. With this method, we detect almost 13 000 15 min totally overcast periods used to derive CRE_{SW} and CRE_{LW}.

3 Parameterization of the instantaneous cirrus cloud radiative effect on surface-level at regional scale

Cirrus cloud radiative effect estimations require precise references of solar and infrared irradiances for the cloud-free atmosphere. In fact, the cirrus cloud radiative effects at the surface on both shortwave (CRE_{SW}) and longwave irradiances (CRE_{SLW}) are defined as the difference between the shortwave and longwave all-sky measured irradiances and the clear-sky reference values. In this study, clear-sky reference values are obtained from parameterizations fitted directly to observed clear-sky data (e.g., a sky without any liquid water or ice cloud).

ACPD
9, 26777–26832, 2009

3.1 Shortwave radiative effect parameterization

3.1.1 Shortwave clear-sky reference

The shortwave clear-sky reference used in this study corresponds to a parametric equation developed by Dupont et al. (2008). This parametric model has the added merit of accounting for hourly variations of aerosol and water vapor that permit to increase significantly the accuracy of the reference clear-sky values compared to well-known Long and Ackerman (2000) and Dutton et al. (2004) parameterizations. Table 3 shows the Root Mean Square Error (RMSE) and the uncertainty, at the 95% confidence level (Std. Err.), computed from a population of independent clear-sky situations. RMSE=$(\sigma^2+\Delta^2)^{0.5}$, where σ is the standard deviation and Δ is the residual bias and Std. Err.=$2\times\sigma/\sqrt{n}$ where n is the number of independent clear-sky days and σ is the standard deviation of the difference between clear-sky model and measured clear-sky irradiances for each day. The standard error of this parameterization is found to be less than 4 W m^{-2} for each site (3.9 W m^{-2} for the SIRTA, 2.1 W m^{-2} for the SGP, 2.8 W m^{-2} for the TWP and 2.3 W m^{-2} for the NSA site), meaning that any cloud effect on surface shortwave irradiances less than 4 W m^{-2} cannot be considered statistically significant.

3.1.2 Average CRE_{SW}

Cirrus cloud shortwave effect defined as the difference between the measured shortwave downwelling irradiance at the surface and that expected for clear-sky conditions is calculated for each site and for each overcast condition. The average CRE_{SW} equals −28 W m^{-2} for the SIRTA, to −32 W m^{-2} for the SGP, to −38 W m^{-2} for the TWP and to −25 W m^{-2} for the NSA site. The more important values calculated for each site are several hundreds of W m^{-2}, and we note that we have some positive effect with maximum value of +40 W m^{-2}. These last positive values are likely to be induced by the strong forward scattering related to the cirrus cloud ice crystal that increases the

ACPD
9, 26777–26832, 2009

diffuse SW irradiance over that for the clear-sky and the magnitude of the SW direct is that which would occur under clear-sky if cirrus cloud does not mask the solar disk.

Table 4 shows the average CRE_{SW} for each cirrus cloud class according to their cloud optical thickness and their cloud base height. The CRE_{SW} associated to low-altitude cirrus clouds are more important for the SIRTA and SGP sites (-58 and $-53\,W\,m^{-2}$) than for the TWP and the NSA sites (-34 and $-40\,W\,m^{-2}$) due to thicker clouds over mid-latitude sites: much more important when considering low-level thick cirrus clouds (CBH<7 km and COT>0.3). Subvisible cirrus clouds have no significant impact except for the SGP site (CBH>11 km) and for the NSA site (9 km<CBH<11 km). Thick cirrus clouds (COT>0.3) have a much stronger CRE_{SW} (about $-95\,W\,m^{-2}$) than subvisible (about $0\,W\,m^{-2}$) and semi-transparent cirrus clouds (about $-17\,W\,m^{-2}$). The altitude of cirrus cloud occurrence is less significant (low: about $-46\,W\,m^{-2}$, medium: about $-35\,W\,m^{-2}$, and high: about $-13\,W\,m^{-2}$). These average values depend on sampling for each site and can be affected by the solar zenith angle, the cirrus cloud properties and the aerosol and water vapor content. To quantify the effect of each term on the instantaneous CRE_{SW}, we study for the first time the relationship between CRE_{SW} and the cirrus cloud optical thickness (COT).

3.1.3 COT retrieval method

Cloud optical thickness derived from lidar measurement is affected by the significant extinction of the lidar beam in its path through the medium, and in most situations, one must take into account multiple scattering. Some typical values of multiple scattering factor η, as given by Chen et al. (2002) are η=0.58 for COT=1 and η=0.95 for COT=0.1. Sassen and Comstock (2001) assume that the multiple scattering factor is of 0.9 for subvisible cirrus clouds, of 0.8 for relatively thick clouds, and of 0.6 to 0.7 for optically thick clouds. For this study, we consider the Chen et al. (2002) parametric equation η=COT/exp(COT)−1. The multiple scattering factor ranges between 0.5 and 1.0 with almost 60% higher than 0.9. Figure 1d shows the cumulative occurrence of the

ACPD
9, 26777–26832, 2009

cirrus cloud optical thickness (COT) for each site when forward and multiple scattering are taken into account.

To relate the cirrus cloud optical thickness and CRE_{SW}, it is essential to retrieve cirrus optical thickness along the direct solar path. In fact, cirrus cloud enhances the SW diffuse and decrease larger the SW direct to induce a negative cloud effect. Because of cirrus cloud spatial inhomogeneities, Dupont et al. (2008) developed a method that combines lidar and sun-photometer measurements to retrieve cloud optical thickness along the direct solar path. In overcast situations, the sun-photometer measures a total optical thickness (TOT) that corresponds to the sum between the aerosol optical thickness (AOT) and an estimated cloud optical thickness (COT^*). COT^* is not equal to the true cirrus cloud optical thickness noted COT because a sun-photometer (with a finite field-of-view of 2.4°), in cirrus overcast conditions, measures not only the attenuated direct radiance but also the forward scattered radiance, because ice crystals can produce significant forward scattering. Hence, Shiobara et al. (1995) developed a method based on Monte Carlo radiative transfer simulations for multiple scattering in cirrus clouds to establish that $COT=[2.15\pm0.35]\times COT^*$ (used in Dupont et al., 2008). However, in this study, we use the COT calculated by lidar over the SIRTA and the SGP sites to adjust the ratio between COT and COT^*. We also use a long-time period of several hours when the sun-photometer and the lidar work simultaneously to establish the average relationship $COT=[1.27\pm0.12]\times COT^*$.

3.1.4 Relationship between CRE_{SW} and COT

Average relationship

Figure 2 shows a scatter plot of the shortwave cirrus cloud radiative effect (CRE_{SW}) versus COT for all the data sets that correspond to almost 5100 15 min periods. The dotted black line is the best linear fit optimized by the method of the least squares applied on the CRE_{SW} median every 0.1 COT step. The black dot markers correspond to CRE_{SW} median every 0.1 COT step. The slope of this fit is $-118\,W\,m^{-2}\,COT^{-1}$

ACPD
9, 26777–26832, 2009

with a correlation factor of 0.81. If we consider each site independently, the best linear fit is $-106\,W\,m^{-2}\,COT^{-1}$ for the SGP data set, $-115\,W\,m^{-2}\,COT^{-1}$ for SIRTA, $-107\,W\,m^{-2}\,COT^{-1}$ for TWP and $-172\,W\,m^{-2}\,COT^{-1}$ for NSA.

The much more important slope for the NSA site is likely to be induced by the particular distribution of the crystal geometry of cirrus cloud composed of polar stratospheric clouds (Noël et al., 2008). In fact, the slope reaches $-202\,W\,m^{-2}\,COT^{-1}$ if we consider only cirrus clouds higher than 7 km high.

Solar illumination geometry effect

The cirrus cloud effects on surface solar irradiance can also be modulated by the solar illumination geometry, here represented by the solar zenith angle (SZA). The relative contribution of the diffuse irradiance to the total shortwave increases with the solar zenith angle (both the diffuse and direct decrease with increasing SZA, but the direct decreases more rapidly). Hence, for a given cloud optical thickness, CRE_{SW} is less important when SZA increases because of the more important effect of cirrus cloud on direct irradiance. To establish the relationship between CRE_{SW} and SZA, we divided the data set into classes of SZA and we calculate for each class the slope between CRE_{SW} and COT noted here as CRE_{SW*}. Figure 3 shows the scatter plot of the CRE_{SW*} versus the cosine of SZA noted cos(SZA). The red line is the best polynomial fit optimized by the method of the least squares applied on the CRE^{*}_{SW} median every 0.05cos(SZA) step. The black dot markers correspond to the CRE_{SW*} median every 0.05cos(SZA) step. This polynomial fit noted $P_{(cSZA)}$ is developed in Eq. (1) and accounts for the significant impact of solar illumination on the cirrus cloud effect: for a given cloud optical thickness equals to unit, the surface-level SW impact can range from $-36.6\,W\,m^{-2}$ (for a sun in the zenith) to $-137\,W\,m^{-2}$ (for a sun near the horizon). The R^2 value of 0.97 for this P fit indicates the strong relationship between CRE^{*}_{SW} and SZA. Hence, the CRE_{SW*} slope is optimized for each situation depending on the solar illumination and is adjusted every 15 min period on the SZA value. The average slope of $-118\,W\,m^{-2}\,COT^{-1}$ for all the data sets correspond to a solar zenith angle of 63°.

ACPD
9, 26777–26832, 2009

Aerosol and humidity effect

Aerosol and water vapor located between the ground surface and the cirrus cloud base also can modulate the cirrus cloud effects on surface solar irradiance. To quantify these variables, we consider the combined effect of aerosol and water vapor rather than each parameter independently. We also use the aerosol optical thickness (AOT) and the water vapor optical thickness (WVOT). WVOT is derived from IWV using the parametric equation established by Darnell et al. (1988) and Lacis and Hansen (1974). In fact, we note that the sum (AOT+WVOT) has a statistically more significant impact on CRF_{SW*}. Here, we evaluate the (AOT+WVOT) radiative effect, that we usually name atmospheric turbidity, on the CRE_{SW*} residual (ΔCRE_{SW*}) previously adjusted with cos(SZA). Figure 4 shows a scatter plot of the sensitivity of CRE_{SW*} residual (ΔCRE_{SW*}) versus the turbidity (AOT+WVOT). The red line is the best linear fit optimized by the method of the least squares applied on the ΔCRE_{SW*} median every 0.02AOT+WVOT step. The black dot markers correspond to the ΔCRE_{SW*} median every 0.02AOT+WVOT step. Equation (1) presents the $P_{1(AOT+WVOT)}$, which is the parametric equation that accounts for the turbidity variability in the calculation of the cirrus cloud radiative forcing at the surface. ΔCRE_{SW*} ranges from $44\,W\,m^{-2}\,COT^{-1}$ to $-40\,W\,m^{-2}\,COT^{-1}$ for unrealistic totally pristine atmosphere (AOT+WVOT=0) and turbid atmosphere (AOT+WVO=0.5), respectively. The R^2 value of 0.85 for this P_1 fit indicates the strong relationship between CRE^*_{SW} and the turbidity of the atmosphere. The neutral turbidity value for this fit equals 0.27, which corresponds to medium atmosphere in terms of aerosol and water vapor contents.

CRE_{SW} parameterization and uncertainties

Figures 3 and 4 exhibit the statistically significant effect of the solar illumination (SZA) and the turbidity (AOT+WVOT) on the cirrus cloud solar radiative effect, respectively.

ACPD
9, 26777–26832, 2009

Equation (1) illustrates the different equations taking into account these variables necessary to quantify as precisely as possible the CRE_{SW} every 15 min periods over each site.

$$\begin{aligned} CRE_{SW} &= CRE_{SW} * \times COT \\ \text{and} \quad CRE_{SW} &= P_{(cSZA)} + P_{1(AOT+WVOT)} \\ \text{with} \quad P_{(cSZA)} &= -222.1 \times cSZA^3 + 480.7 \times cSZA^2 - 358.0 \times cSZA - 36.6 \\ \text{and} \quad P_{1(AOT+WVOT)} &= -166.1 \times (AOT + WVOT) + 44.2 \end{aligned} \tag{1}$$

However, based on radiative transfer calculations, Schlimme et al. (2004) and Wendisch et al. (2005) show that the sensitivity of downwelling shortwave irradiance to cloud optical thickness is modulated by 10 to 30% as a result of ice crystal geometry, and ice particle size in cirrus clouds. Similarly our methodology to derive cirrus cloud optical thickness assigns a ±10% uncertainty in their forward scattering correction function. The two polynomial fits $P_{(CSZA)}$ and $P_{(AOT+WVOT)}$ are associated with a R^2 factor of 0.97 and 0.85, respectively. The Eq. (1) is also characterized by a R^2 factor between measured and estimated CRE_{SW} of 0.72. Table 5 illustrates the accuracy of this parameterization with is a contingency table that shows CRE_{SW} estimated using our methodology and the CRE_{SW} measured at the ground-level for all the data sets (15 min period data). Here, 19.2% of the entire negative observed CRE_{SW} has a very little impact between 0 and $-10\,W\,m^{-2}$, 44.6% between -10 and $-50\,W\,m^{-2}$, and finally 36.2% higher than $-50\,W\,m^{-2}$. We note a good agreement between observed and estimated CRE_{SW} with almost 60% of perfect agreement in the diagonal of this table. However, only 2.4% cases show a -50 or more $W\,m^{-2}$ difference between estimated and estimated CRE_{SW}.

ACPD
9, 26777–26832, 2009

3.2 Longwave radiative effect parameterization

3.2.1 Longwave clear-sky reference

Longwave clear-sky reference used in this study corresponds to parametric equation developed by Dupont et al. (2007). This parametric model considers that the atmosphere is a grey body and that LW clear-sky values can be estimated by Stephan-Boltzmann's law (Angström 1918, Brunt 1932, Swinbank 1963. Apparent clear-sky emissivity of the atmosphere is expressed as a function of surface air temperature, water vapor pressure near surface, vertical distribution of humidity, and the time lag between surface and atmosphere heating and cooling in the diurnal cycle. The standard error of this parameterization is found to be less than 2.8 $W\,m^{-2}$ for each site (1.4 $W\,m^{-2}$ for SIRTA, 1.8 $W\,m^{-2}$ for SGP, 1.8 $W\,m^{-2}$ for TWP and 2.8 $W\,m^{-2}$ for NSA sites), meaning that any cloud effect on surface longwave irradiances less than 3 $W\,m^{-2}$ cannot be considered statistically significant (Table 6).

3.2.2 Average CRE_{LW}

The cirrus cloud longwave effect, defined as the difference between the measured longwave downwelling irradiance at the surface and that expected for clear-sky conditions, is calculated for each site and for each overcast condition. The average CRE_{LW} is equal to +6 $W\,m^{-2}$ for SIRTA, to +9 $W\,m^{-2}$ for SGP, to +0.8 $W\,m^{-2}$ for the TWP site, and to +5.1 $W\,m^{-2}$ for the NSA site. Results are statistically significant except for the TWP site characterized by a CRF_{LW} near 0 $W\,m^{-2}$. These average values are modulated by the sampling for the cirrus cloud and the atmospheric properties over each site. To quantify the effect of each term on the instantaneous CRE_{LW}, we study the relationship between CRE_{LW} and the cirrus cloud infrared emissive power.

Table 7 shows the CRE_{LW} for each cirrus cloud class according to cirrus cloud optical thickness and cloud base height. The CRE_{LW} associated with high-altitude cirrus clouds are statistically different from 0 for the SIRTA and the SGP sites, 2.5 and

ACPD
9, 26777–26832, 2009

5.2 W m^{-2}, respectively. Low-altitude cirrus clouds, however, produce significant effects on the surface longwave irradiances at 14.3, 10.4, and 8.7 W m^{-2} for the SIRTA, SGP and NSA sites. For the TWP site, the low-level thick cirrus clouds yield significant effects on surface longwave irradiances (2.8 W m^{-2}). For high-level cirrus clouds in particular, the subvisible class yields significant effects on surface longwave irradiances at the SGP site (2.5 W m^{-2}).

3.2.3 Relationship between CRE_{LW} and LW_{cirrus}

The longwave irradiance emitted by the cirrus cloud is noted LW_{cirrus} and is computed from Stephan-Boltzmann's law based on the cirrus cloud infrared emissivity and thermodynamic temperature inside the cirrus cloud. The cloud infrared emissivity is derived from the cloud optical thickness based on a parametric relationship (e.g., Rossow et al., 1996). The cloud thermodynamic temperature is derived by combining radiosonde and lidar measurements that provide temperature profiles and cloud mean altitude, respectively. Temperatures are interpolated between radiosoundings at the time and altitude of lidar observations.

Because water vapor is an efficient absorber of longwave radiation and water vapor content is highly variable on synoptic and seasonal scales, measured CRE_{LW} is likely to be affected by the water vapor content of the atmosphere between surface and cloud base. Figure 5 shows the scatter plot of the longwave cirrus cloud effect (CRE_{LW}) versus cirrus cloud emissive power for the data collected in all the sites. The colored area represents the integrated water vapor content. The black line corresponds to the best linear fit adjusted on the 50% wettest atmosphere and the dashed black line to the 50% driest atmosphere. The average integrated water content is 2.6 cm for all the data sets. The slopes representing the driest and the wettest cases equal 0.02 and 0.15, respectively. That means that about 15% of the LW irradiance emitted by the cirrus cloud is received at the ground for the driest cases and only 2% for the wettest.

ACPD
9, 26777–26832, 2009

This slope is noted CRE_{LW*}. The R^2 value of 0.51 and 0.63 for each case shows a significant impact of water vapor on the infrared opacity of the atmosphere.

The results of the Figure 5 show a very important scattering around the mean slope and encourage considering a more representative parameter named γ and expressed in Eq. (2). In this equation, ε is the cirrus cloud infrared emissivity, T the surface air temperature in Kelvin, e the water vapor pressure near surface in hPa, and IWV the integrated water content in g cm^{-2}. The term $(e/T)^2$/IWV accounts for at the same time of the absolute value of the water vapor content in the atmosphere and the vertical distribution of water vapor. In fact, a high value of this term means that the humidity is more concentrated near the ground than in the average profile and a low value means that the vertical distribution of humidity is weighted higher in the atmosphere (Dupont et al., 2007). For a similar integrated water vapor, a more distributed water vapor along the vertical induces a smaller infrared mask. Also, we consider cirrus cloud emissivity in γ term to account for the fact that the cirrus cloud does not exactly emit like a gray body. The vertical extension of the cirrus cloud induced an emissive power coming from particles between cloud base and cloud top that is not precisely equal to the integrated emissivity multiplied by the average temperature of the cirrus cloud. When cirrus cloud emissivity increases, we tend to decrease the infrared transmissivity to correct the fact that cirrus clouds do not emit exactly like a gray body.

Figure 6 shows the scatter plot of the sensitivity of CRE_{LW*} versus γ parameter. The red line is the best polynomial fit optimized by the method of the least squares applied on the CRE_{LW*} median every 0.02γ step. The black dot markers correspond to the CRE_{LW*} median every 0.02γ step. R^2 value of 0.92 shows the strong relationship between the cirrus cloud infrared radiative effect and the water vapor. For a totally dry atmosphere or totally wet atmosphere, CRF_{LW*} is 0.32 or 0.02, respectively.

ACPD
9, 26777–26832, 2009

3.2.4 CRE_{LW} parameterization and uncertainties

Equation (2) sums up the methodology used to quantify the cirrus cloud effect on longwave irradiance measured at the surface. We present the definition of the $CRE_{LW}*$, the parametric equation associated with, and the γ term used in the calculation.

$$CRE_{LW} = CRE_{LW}* \times LW_{cirrus}$$
$$\text{and} \quad CRE_{LW}* = -0.13 \times \gamma^3 + 0.51 \times \gamma^2 - 0.63 \times \gamma + 0.32$$
$$\text{with} \quad \gamma = \frac{\varepsilon \times \left(\frac{e}{T}\right)^2}{IWV} \times 10000 \qquad (2)$$

Uncertainties in the relationship between CRE_{LW} and LW_{cirrus} are due to the following factors: LW irradiance measurement uncertainties (1–2%), clear-sky parametric model uncertainties (1%), and cloud emissivity (±15%) and temperature (2%) uncertainties. As a result the uncertainty in the relationship between CRE_{LW} and LW_{cirrus} can be estimated to be 20%, which is close to the empirical standard error (17%). The Eq. (2) is also characterized by a R^2 factor between measured and estimated CRE_{LW} of 0.62. Table 8 illustrates the accuracy of the CRR_{LW} parameterization with is a contingency table that shows CRE_{LW} estimated using our methodology and the CRE_{LW} measured at the ground-level for all the data sets (15 min period data). Here, 39.8% of the entire positive observed CRE_{LW} have a very little impact between 0 and 5 $W\,m^{-2}$, 29.8% between 5 and 10 $W\,m^{-2}$, and finally 30.3% higher than 10 $W\,m^{-2}$. We note a good agreement between observed and estimated CRE_{SW} with almost 52% of perfect agreement in the diagonal of this table. The average estimated CRE_{LW} is +0.5 $W\,m^{-2}$ stronger than the measured CRE_{LW}. Moreover, measured CRE_{LW} is characterized by a wider distribution including negative CRE_{LW} and much stronger CRE_{LW}.

ACPD
9, 26777–26832, 2009

4 Instantaneous and cumulative cirrus cloud radiative effect variability

Cirrus cloud optical thickness values used to adjust Eqs. (1) and (2) are collocated with the SW and LW downwelling irradiance at the ground-level. However, the method developed and explained in Sect. 3.1.3 significantly limits the sampling over each site. Hence, in this section, we used directly the equations 1 and 2 providing CRE_{SW} and CRE_{LW} starting from cirrus cloud properties and atmospheric composition. To significantly increase the data set and be able to study the annual variability of cirrus cloud effect, we derive the cirrus cloud optical thickness from lidar observations (Morille et al., 2007; Cadet et al., 2005) rather than AERONET. Cloud optical thickness is retrieved for cloud layers using a standard transmission-loss algorithm (Platt, 1973).

This method, based on backscatter signal measured by ground-based lidar, is used only for the SIRTA and SGP sites because the COT product is not available with the micropulse lidar installed at the TWP and NSA sites. For the TWP site, the very high occurrence of cirrus clouds (>50% of occurrence) allows us to use the methodology developed in Sect. 3.1.3. However, for the NSA site, we do not present the annual cycle cirrus effect because of the too-limited monthly sampling. These results are presented in Sect. 4.1, whereas Sect. 4.2 uses as input parameters the spatial data provided by CALIOP and AIRS.

4.1 Monthly variations at regional scale

4.1.1 Instantaneous effect

The term "instantaneous effect" corresponds only to the radiative impact when the cirrus clouds are present over each site. The monthly means of the LW, SW, and NET cirrus cloud instantaneous radiative effect for the SGP, SIRTA, and TWP sites are illustrated in Fig. 7, and their seasonal means are summarized in Table 9. CRE_{NET}, the sum of SW and LW cirrus cloud radiative effect, are determined primarily by CRE_{SW} throughout most of the year. During winter, however, the negative CRE_{SW} and positive

ACPD
9, 26777–26832, 2009

CRE_{LW} nearly cancel each other, resulting in CRE_{NET} of −7 and −7.6 W m^{-2} for the SIRTA and SGP sites. CRE_{LW} over the SGP site has a significant annual cycle, due to the important range of water vapor (Fig. 1) inducing an important range of CRE_{LW}*, with the value ranging between 18.3 W m^{-2} to 10.7 W m^{-2} in winter and summer, respectively. CRE_{SW} is a little bit higher in summer over the SGP and SIRTA sites (+10–15 W m^{-2} of radiative impact during summer compared to winter period) in correlation with a smaller solar zenith angle (synonymous of a higher CRF_{SW}*, Fig. 3). Finally, we note a net positive impact in February (7 W m^{-2}) and near 0 W m^{-2} in March and December (−1.1 and −0.2 W m^{-2}) over the SGP site and of 0.3 W m^{-2} in November over the SIRTA site. Cirrus net effect over the TWP site is composed mainly of the SW effect (seasonal average ranging from −49 to −16 W m^{-2}) because of the very limited LW effect (annual average of 1.0 W m^{-2}). The water vapor mask is much more significant over the tropical region (Figs. 1 and 6). The results concerning the SGP site are similar to Dong et al. (2005) showing a CRE_{SW} of −37 W m^{-2} (−33 W m^{-2} here) and a CRE_{LW} of 17 W m^{-2} (here 15.1 W m^{-2}). A little more important impact observed by Dong et al. (2005) must be induced by the taking into account of cirrus clouds higher than 6 km (7 km in our study). Shupe and Intrieri (2003) quantify the annual CRE_{SW} and CRE_{LW} reach −3 and 16 W m^{-2}, respectively, over an Artic site. Statistics obtained over the SGP site seems to confirm this positive net impact for the dry and cold region (net CRE of 7 W m^{-2} in February).

4.1.2 Cumulative effect

The relative importance of the cirrus clouds in the current climate radiation budget also depends on their abundance. In fact, as shown by Chen et al. (2000) the very strong cloud fraction of the cirrus cloud induced a "cumulative" CRE_{SW} and CRE_{LW} stronger than low level-clouds. In our study, the term "cumulative" is defined as the cirrus cloud instantaneous effect "normalized" for all-sky and for all-time. In this section, we calculate the cloud fraction using the lidar signal over each site. Cloud fraction corresponds

ACPD
9, 26777–26832, 2009

here to the ratio between the number of vertical profiles with the presence of cirrus cloud and the total number of vertical profiles during 1 h period. Cloud fraction ranges from 0 to 100% and the average cloud fraction is 25.6%, 49%, 43.5% for the SGP, SIRTA and TWP sites, respectively. The cloud fraction is processed for the daytime and nighttime periods; the latter was only used for the LW cirrus cloud radiative impact. The SIRTA backscatter lidar operated exclusively during the daytime periods, which is why we consider a similar value for daytime and nighttime for this site.

The LW cirrus cloud radiative effect appears all the time, day and night, whereas the SW effect is effective only during the sunshine period. Here, we use the time equation developed by Angström (1924) to calculate the sunshine duration period over each site for every cirrus cloud effect. We define the sunshine duration ratio as the ratio between sunshine duration period in hours and 24. Hence, the cumulative cirrus cloud effect equals the instantaneous CRE_{SW} (CRE_{LW}) multiplied by the cloud fraction and the sunshine duration ratio (we calculate a day and night CRE_{LW}).

The monthly means of the LW, SW, and NET cirrus cloud cumulative radiative effect for the SGP, SIRTA and TWP sites are illustrated in Fig. 8, and their seasonal means are summarized in Table 10. The negative CRE_{SW} and the positive CRE_{LW} are much more similar than for the instantaneous impact (Fig. 9). We show that maximum monthly cumulative CRE_{NET} reaches $4\,W\,m^{-2}$ in February and March at the SGP site, $3\,W\,m^{-2}$ in November and February at the SIRTA site, and $-2\,W\,m^{-2}$ in October at the TWP site. For seasonal average, we note a positive cumulative net cirrus effect during winter and autumn at the SGP and SIRTA sites ranging from 0 to $4.8\,W\,m^{-2}$. The seasonal average cumulative SW cirrus effect ranges from -2.3 to $-7.6\,W\,m^{-2}$ at the SGP site (winter and summer period), from -17.1 to $-5.4\,W\,m^{-2}$ at TWP site (winter and autumn), and from -12.6 to $-3.8\,W\,m^{-2}$ at SIRTA site (spring and autumn).These results are comparable with Chen et al. (2000) that find a global mean CRE_{SW} of $-3.6\,W\,m^{-2}$ with a peak near the tropics at $-8\,W\,m^{-2}$. Moreover, they show an all-cloud CRE_{SW} (CRE_{LW}) of $-52.6\,W\,m^{-2}$ ($24.4\,W\,m^{-2}$) that implies a significant contribution of cirrus clouds.

ACPD
9, 26777–26832, 2009

4.2 Seasonal and zonal variations at global scale

In the following analyses, we use our parameterizations and satellite-derived input data to calculate the zonal means seasonal and zonal variations of cirrus cloud radiative effect at global scale. CRE is processed twice a day, both daytime and nighttime periods, that provide almost 500 overpasses with about 45 samples each. Over each site, the cloud fraction is equal to the ratio between the number of samples where cirrus clouds are detected and the total number of samples at each overpass. The cloud fraction is focused on situations where cirrus clouds are present without cloud below (almost 80% of the lidar signal reaches the surface allowing a correct identification of low level clouds).

4.2.1 Instantaneous effect

Figure 9 shows the zonal cirrus clouds instantaneous effect at the surface for the different seasons: (A) winter, (B) spring, (C) summer and (D) autumn; and their average for five latitude classes are presented in Table 11 (75° S to 45° S zone, 45° S to 15° S zone, 15° S to 15° N zone, 15° N to 45° N zone, and 45° N to 75° N zone). Note that in the Figs. 11 and 12, SW, LW, and NET CRE are not plotted because cirrus cloud properties are unavailable. The study is limited to the latitude range 75° S–75° N. The seasons considered here are defined as the seasons in the Northern Hemisphere. The global mean values are −16.6, 7.7, and −8.8 $W m^{-2}$ for CRE_{SW}, CRE_{LW}, and CRE_{NET}, respectively. Results obtained by Chen et al. (2000) are relatively similar with the global mean of −22.4, 8 and −14.2 $W m^{-2}$ for CRE_{SW}, CRE_{LW}, and CRE_{NET}. Figure 11 shows the significant variability of the cirrus cloud radiative effect at global scale. With the decreasing sunlight and water vapor contained during winter and autumn season particularly near the Poles, the CRE_{SW} is near 0 $W m^{-2}$ and the CRE_{LW} reaches almost 10 $W m^{-2}$. Hence, in the 45–75° N zone, CRE_{NET} ranges from −5.2 $W m^{-2}$ in summer to 3.6 $W m^{-2}$ in autumn. The cirrus cloud radiative effect reaches 0.9 between 15° N and 45° N in winter period, whereas it is −13.7 $W m^{-2}$ during summer period. In

ACPD
9, 26777–26832, 2009

the south hemisphere, the positive effect of cirrus cloud is significant only starting from 60° S in winter and in spring reaching 3 W m^{-2} at 65° S. However, the net annual zonal mean impact is equal to −4.5 W m^{-2}. Near the equator, where the water vapor opacity is largest, the CRE_{LW} is limited and ranges from 6.3 W m^{-2} (summer) to 10.1 W m^{-2} (spring). CRE_{LW} reaches 15 W m^{-2} near 30° N and 30° S in winter and spring. These more important values also are related to the cirrus cloud base altitude that is lower at 30° S and 30° N than near the equator. The general latitude dependencies concerning the decreasing temperatures and humidity with latitude induced a CRE_{LW} more important relative to the CRE_{SW}.

4.2.2 Cumulative effect

Figure 10 and Table 12 are similar to Fig. 11 and Table 11, but for the cumulative cirrus cloud radiative effect. To calculate the cumulative cirrus cloud effect, we calculate for each 2.5°×2.5° the cloud fraction and the sun-shine duration. Cirrus cloud fraction (not shown here) reaches almost 60% near the equator, 30% for 30–60° N and 25% for 30–60° S. These cloud fractions are more important than Chen et al. (2000) because we consider here all the cirrus cloud data sets whereas Chen et al. (2000) used the ISCCP classification (Rossow et al., 1996): only the cirrus cloud optical thickness higher than 0.1 was considered. The global mean values of the cumulative CRE are −2.8, 1.7, and −1.1 W m^{-2} for CRE_{SW}, CRE_{LW}, and CRE_{NET}, respectively. Chen et al. (2000) showed an impact of −3.6, 1.1, and −2.5 W m^{-2}. The main difference come from the definition of the cumulative effect, which is defined without accounting for the sunshine duration that tends to increase the CRE_{SW} and minimize the CRE_{LW}. Decreasing the sunlight duration during the winter induces a net positive CRE starting from 20° N and 30° N for the autumn reaching a maximum of 0.8 W m^{-2}. The CRE_{LW} is maximum near the equator, with 1.5 W m^{-2}, due to the much more important cloud fraction that compensates the strong water content in this region. However, the net effect is negative in this region related to the strong CRE_{SW}. The seasonal average of CRE_{SW} is relatively

constant for the 15° S–15° N zone (average value of $-5.2\,W\,m^{-2}$), whereas the range is much more significant for 15–45° S ($-4.1\,W\,m^{-2}$ in winter and $-2.0\,W\,m^{-2}$ in summer) and for 15–45° N ($-1.3\,W\,m^{-2}$ in winter and $-4.8\,W\,m^{-2}$ in summer). This range is related to the ITCZ variability that induced important changes in the cirrus cloud fraction in North and South hemisphere.

5 Conclusions and perspectives

In this paper, we derive (1) the sensitivity of surface CRE_{SW} to the cloud optical thickness modulated by the solar zenith angle and the atmospheric turbidity (noted $CRE_{SW}*$) and (2) the sensitivity of surface CRE_{LW} to the infrared emissive power of cirrus cloud modulated by the water vapor content (noted $CRE_{LW}*$). The average $CRE_{SW}*$ is $-120\,W\,m^{-2}\,COT^{-1}$ but it ranges from -80 to $-140\,m^{-2}\,COT^{-1}$ depending on the solar illumination with residual variability ranges from +40 and $-40\,W\,m^{-2}\,COT^{-1}$ from pristine to turbid conditions, respectively. We also have established one parametric equation that accounts for this variability, considering SZA and water vapor and aerosol optical thickness as input parameter. The $CRE_{LW}*$, that corresponds to the infrared transmissivity of the atmosphere, ranges from 3% to 40% from dry to wet atmospheric conditions, respectively, and is also parameterized.

The four ground-based sites displayed significant differences concerning CRE_{SW} and CRE_{LW} annual average and the seasonal variability. The mid-latitude ARM SGP site presents a seasonal mean CRE_{LW}, which is greatest during the winter ($18\,W\,m^{-2}$) and least during the summer ($10\,W\,m^{-2}$) due to water vapor mask and annual cycle of cirrus cloud base altitude dependency. The tropical ARM TWP site displayed quasi-null CRE_{LW} with annual average value about $1\,W\,m^{-2}$ related to strong water vapor content. The subvisible cirrus class (COT<0.03) over mid-latitude sites, which represents 20% of the population, induces a significant increase in surface LW irradiance at the 2–$7\,W\,m^{-2}$ level. The semi-transparent cirrus class (0.03<COT<0.3), which represents

ACPD
9, 26777–26832, 2009

45% of the population, will affect the surface SW irradiance by −12 to −25 W m^{-2}. The SW radiative impact of medium altitude cirrus clouds (9–11 km) ranges from −20 to −45 W m^{-2}, while that of the thicker cirrus (0.3<COT<3) is greater than 95 W m^{-2} on average.

Cumulative CRE accounts for sunshine duration and cirrus cloud occurrence and has the merit to quantify the real impact precisely at the surface ground-level to study the surface radiation budget. Mid-latitude sites are characterized by a net warming in the winter season induced by cirrus clouds reaching 2.8 and 1.8 W m^{-2} for the SGP and SIRTA sites, respectively with an summer cumulative CRE_{NET} near −4 W m^{-2}. The Nauru site average cumulative CRE_{NET} equals −10 W m^{-2} in relation with a very small cirrus cloud warming due to high water vapor content.

Global CRE estimations show very significant zonal and seasonal variability of each component of the CRE_{NET}. The CRE_{NET} is 0.4 W m^{-2} during winter/autumn for 15–75° N and 1 W m^{-2} for 45–75° S, whereas it is near −3 W m^{-2} for 15° S–15° N (major influence of the sunshine duration modulates significantly the ratio CRE_{SW}/CRE_{LW}). The summer period shows a cirrus cloud global cooling at all the latitudes except for 75–45° S with a quasi-null effect and a peak at −3.6 W m^{-2} for 15° S–45° N. The global average cumulative CREs are −2.8, 1.7, and −1.1 W m^{-2} for CRE_{SW}, CRE_{LW}, and CRE_{NET}, respectively. For high latitudes region (tropics), 45–75° N (15° S–15° N) these annual average values are −1.3, 0.9 and −0.4 W m^{-2} (−5.2, 2.4 and −2.8 W m^{-2}), respectively. These important zonal and seasonal CRE values highlight that the cirrus clouds can affect significantly regional and global radiative budget. Cirrus clouds should be considered carefully in climate modeling.

ACPD
9, 26777–26832, 2009

Acknowledgements. The authors would like to thank the Centre National d'Etudes Spatiales (CNES), the Centre National de la Recherche Scientifique (CNRS), and the Climate Change Research Division of the US Department of Energy as part of the Atmospheric Radiation Measurement (ARM) Program for their support in this study. Recognition also is extended to those responsible for the operation and maintenance of the instruments that produced the measurements used in this study; their diligent and dedicated efforts are often underappreciated.

The publication of this article is financed by CNRS-INSU.

References

Ackerman, T. P., Flynn, D. M., and Marchand, R.: Quantifying the magnitude of anomalous solar absorption, J. Geophys. Res., 108, 4273, 2003.

Ackerman, T. P. and Stokes, G. M.: The atmospheric radiation measurement program, Phys. Today, 56, 38–44, 2003.

Angström, A.: A study of the radiation of the atmosphere, Smithson. Misc. Collect., 65, 1–159, 1918.

Angström, A.: Solar and terrestrial radiation, Q. J. Roy. Meteorol. Soc., 50, 121–125, 1924.

Aumann, H. H., Chahine, M. T., Gautier, C., Goldberg, M. D., Kalnay, E., McMillin, L. M., Revercomb, H., Rosenkranz, P. W., Smith, W. L., Staelin, D. H., Strow, L. L., and Susskind, J.: AIRS/AMSU/HSB on the Aqua mission: design, science objectives, data products, and processing systems, IEEE T. Geosci. Remote, 41, 253–264, 2003.

Barkstrom, B. R. and Smith, G. L.: The earth radiation budget experiment: science and implementation, Rev. Geophys., 24, 379–390, 1986.

Brunt, D.: Notes on radiation in the atmosphere, Q. J. Roy. Meteorol. Soc, 58, 389–420, 1932.

Cadet, B., Giraud, V., Haeffelin, M., Keckhut, P., Rechou, A., and Baldy, S.: Improved retrievals

of cirrus cloud optical properties using a combination of lidar methods, Appl. Optics, 44, 1726–1734, 2005.
Cess, R. D., Potter, G. L., Blanchet, J.-P., Boer, G. J., Del Genio, A. D., et al.: Intercomparison and interpretation of climate feedback processes in 19 atmospheric general circulation models, J. Geophys. Res., 95, 16601–16615, 1990.
Cess, R. D., Zhang, M. H., Ingram, W. J., Potter, G. L., et al.: Cloud feedback in atmospheric general circulation models: an update, J. Geophys. Res., 101, 12791–12794, 1995.
Chen, T., Rossow, W. B., and Zhang, Y.: Radiative effects of cloud-type variations, J. Climate, 13, 264–286, 2000.
Chen, W. N., Chiang, C. W., and Nee, J. B.: Lidar ratio and depolarisation ratio for cirrus clouds, Appl. Optics, 31, 6470–6476, 2002.
Choi, Y.-S. and Ho, C.-H.: Radiative effect of cirrus with different optical properties over the tropics in MODIS and CERES observations, Geophys. Res. Lett., 33, L21811, doi:10.1029/2006GL027403, 2006.
Clements, W. E., Barnes, F. J., Jones, L., Ackerman, T. P., Mather J. H., Ivey, M., Lefale, P., Pitcher, A., Cain, J., and Koontz, A.: Nauru: The Second ARM Tropical Western Pacific Site, Proceedings of the Ninth ARM Science Team Meeting, San Antonio, 1999.
Currey, J. C., Tremas, T., Winker, D. M., and Pelon, J.: Cloud-Aerosol LIDAR Infrared Pathfinder Satellite Observations, Data Management System, Data Products Catalog, Document No: PC-SCI-503, 2007.
Darnell, W. L., Staylor, W. F., Gupta, S. K., and Denn, F. M.: Estimation of surface insolation using sun-synchronous satellite data, J. Climate, 1, 820–835, 1988.
Dessler, A. E. and Yang, P.: The distribution of tropical thin cirrus clouds inferred from Terra MODIS data, J. Climate, 16, 1241–1247, 2003.
Divakarla, M. G., Barnet, C. D., Goldberg, M. D., McMillin, L. M., Maddy, E., Wolf, W., Zhou, L., and Liu, X.: Validation of atmospheric infrared sounder temperature and water vapor retrievals with matched radiosonde measurements and forecasts, J. Geophys. Res., 111, D09S15, doi:10.1029/2005JD006116, 2006.
Dong, X., Xi, B., and Minnis, P.: A climatology of midlatitude clouds from the ARM SGP central facility, Part II: cloud fraction and surface radiative forcing, J. Climate, 19, 1765–1783, 2005.
Dupont, J.-C., Haeffelin, M., Drobinski, P., and Besnard, T.: Parametric model to estimate clear-sky longwave irradiance at the surface based on vertical distribution of humidity and temperature, J. Geophys. Res., 113, D07203, doi:10.1029/2007JD009046, 2007.

Dupont, J.-C. and Haeffelin, M.: Observed instantaneous cirrus radiative effect on surface level shortwave and longwave irradiances, J. Geophys. Res., 113, D21202, doi:10.1029/2008JD009838, 2008.
Dupont, J.-C., Haeffelin, M., and Long, C. N.: Evaluation of cloudless-sky periods detected by shortwave and longwave algorithms using lidar measurements, Geophys. Res. Lett., 35, L10815, doi:10.1029/2008GL033658, 2008.
Dupont, J.-C., Chervet, P., Comstock, J., Haeffelin, M., Keckhut, P., Morille, Y., Noël, V., Roblin, A., and Winker, D.: Macrophysical and optical properties of midlatitude cirrus clouds from 4 ground-based lidars and collocated CALIOP observations, J. Geophys. Res., in press, doi:10.1029/2009JD011943, 2009.
Dürr, B. and Philipona, R.: Automatic cloud amount detection by surface longwave downward radiation measurements, J. Geophys. Res., 109, D05201, doi:10.1029/2003JD004182, 2004.
Dutton, E. G., Farhadi, A., Stone, R. S., Long, C. N., and Nelson, D. W.: Long-term variations in the occurrence and effective solar transmission of clouds as determined from surface-based total irradiance observations, J. Geophys. Res., 109, D03204, doi:10.1029/2003JD003568, 2004.
Haeffelin, M., Barthès, L., Bock, O., Boitel, C., Bony, S., Bouniol, D., Chepfer, H., Chiriaco, M., Cuesta, J., Delanoë, J., Drobinski, P., Dufresne, J.-L., Flamant, C., Grall, M., Hodzic, A., Hourdin, F., Lapouge, F., Lemaître, Y., Mathieu, A., Morille, Y., Naud, C., Noël, V., O'Hirok, W., Pelon, J., Pietras, C., Protat, A., Romand, B., Scialom, G., and Vautard, R.: SIRTA, a ground-based atmospheric observatory for cloud and aerosol research, Ann. Geophys., 23, 253–275, 2005, http://www.ann-geophys.net/23/253/2005/.
Haladay, T. and Stephens, G.: Characteristics of tropical thin cirrus clouds deduced from joint CloudSat and CALIPSO observations, J. Geophys. Res., 114, D00A25, doi:10.1029/2008JD010675, 2009.
Hansen, J., Sato, M., and Ruedy, R.: Radiative forcing and climate response, J. Geophys. Res., 102, 6831–6864, 1997.
Harries, J. E., Russell, J. E., Hanafin, J. A., Brindley, H., Futyan, J., et al.: The geostationary earth radiation budget project, B. Am. Meteorol. Soc., 86(7), 945–960, doi:10.1175/BAMS-86-7-945, 2005.
Houghton, J. T., Ding, Y., Griggs, D. J., Noguer, M., van der Linden, P. J., and Xiasu, D.: Climate

Change: The Scientific Basis, Cambridge University Press, 944 pp., 2001.
Lacis, A. A. and Hansen, J. E.: A parameterization for the absorption of solar radiation in the earth's atmosphere, J. Atmos. Sci., 31, 118–133, 1974.
Lee, J., Yang, P., Dessler, A. E., Gaod, B.-C., and Platnicke, S.: Distribution and radiative forcing of tropical thin cirrus clouds, J. Atmos. Sci., 10, 3721–3731, doi:10.1175/2009JAS3183.1, 2009.
Li, Z. and Leighton, H. G.: Global climatologies of solar radiation budgets at the surface and in the atmosphere from 5 years of ERBA data, J. Geophys. Res., 98, 4919–4930, 1993.
Liou, K. N.: Influence of cirrus clouds on weather and climate processes: a global perspective, Mon. Weather Rev., 114, 1167–1199, 1986.
Lo, C., Comstock, J. M., and Flynn, C.: An atmospheric radiation measurements value-added product to retrieve optically thin cloud visible optical depths using micropulse lidar, Rep. DOE/SC-ARM/TR-077, US Dep. of Energy, Washington, DC, 2006.
Long, C. N. and Ackerman, T. P.: Identification of clear skies from broadband pyranometer measurements and calculation of downwelling shortwave cloud effect, J. Geophys. Res., 105, 609–625, 2000.
Long, C. N., Ackerman, T. P., Gaustad, K. L., and Cole, J. N. S.: Estimation of fractional sky cover from broadband shortwave radiometer measurements, J. Geophys. Res., 111, D11204, doi:10.1029/2005JD006475, 2006.
Mace, G., Benson, S., and Kato, S.: Cloud radiative forcing at the atmospheric radiation measurement program climate research facility: 2. vertical redistribution of radiant energy by clouds, J. Geophys. Res., 111, D11S91, doi:10.1029/2005JD005922, 2006.
Morille, Y., Haeffelin, M., Drobinski, P., and Pelon, J.: STRAT: an automated algorithm to retrieve the vertical structure of the atmosphere from single-channel lidar data, J. Atmos. Ocean. Tech., 24, 761–775, 2007.
Nazaryan, H., McCormick, M. P., and Menzel, W. P.: Global characterization of cirrus clouds using CALIPSO data, J. Geophys. Res., 113, D16211, doi:10.1029/2007JD009481, 2008.
Noel, V., Hertzog, A., Chepfer, H., and Winker, D. M.: Polar stratospheric clouds over Antarctica from the CALIPSO spaceborne lidar, J. Geophys. Res., 113, D02205, doi:10.1029/2007JD008616, 2008.
Platt, C. M. R.: Lidar and radiometric observations of cirrus clouds, J. Atmos. Sci., 30, 1191–1204, 1973.
Ramanathan, V., Cess, R. D., Harrison, E. F., Minnis, P., Barkstrom, B. R., Ahmad, E., and

Hartmann, D.: Cloud radiative forcing and climate: results from the earth radiation budget experiment, Science, 243, 57–63, 1989.
Rossow, W. B., Walker, A. W., Beuschel, D., and Roitier, M.: International Satellite Cloud Climatology Project (ISCCP): Description of new Cloud Dataset. WMO/TD-737, World Climate Research Programm (ICSU and WMO), Geneva, Switzerland, 115 pp., 1996.
Sassen, K. and Comstock, J.: A midlatitude cirrus cloud climatology from the facility for atmospheric remote sensing, Part III: Radiative Properties, J. Atmos. Sci., 58, 2113–2127, 2001.
Sassen, K. and Campbell, J. R.: A midlatitude cirrus cloud climatology from the facility for atmospheric remote sensing: I, macrophysical and synoptic properties, J. Atmos. Sci., 58, 481–496, 2001.
Sassen, K., Wang, Z., and Liu, D.: The global distribution of cirrus clouds from CloudSat/CALIPSO measurements, J. Geophys. Res., 113, D00A12, doi:10.1029/2008JD009972, 2008.
Schlimme, I., Macke, A., and Reichardt, J.: The impact of ice crystal shapes, size distributions, and spatial structures of cirrus clouds on solar radiative fluxes, J. Atmos. Sci., 62, 2274–2283, 2004.
Shiobara, M., Spinhirne, J. D., Uchiyama, A., and Asano, S.: Optical depth measurements of aerosol, cloud and water vapor using sun photometers during FIRE Cirrus IFO II, J. Appl. Meteorol., 35, 36–46, 1995.
Stamnes, K., Ellingson, R. G., Curry, J. A., Walsh, J. E., and Zak, B. D.: Review of science issues, deployment strategy, and status for the ARM North slope of Alaska – adjacent arctic ocean climate research site, J. Climate, 12, 46–63, 1998.
Stephens, G. L.: Cloud feedbacks in the climate system: A critical review, J. Climate, 18, 237–273, 2005.
Stubenrauch, C. J., Rossow, W. B., Scott, N. A., and Chédin, A.: Clouds as seen by infrared sounders (3i) and imagers (ISCCP), Part III: spatial heterogeneity and radiative effects, J. Climate, 12, 3419–3442, 1999.
Stubenrauch, C. J., Chedin, A., Rädel, G., Scott, N. A., and Serrar, S.: Cloud properties and their seasonal and diurnal variability from TOVS Path-B, J. Climate, 19, 5531–5553, 2006.
Shupe, M. D. and Intrieri, J. M.: Cloud radiative forcing of the arctic surface: the influence of cloud properties, surface albedo, and solar zenith angle, J. Climate, 17, 616–628, 2003.
Swinbank, W. C.: Long-wave radiation from clear skies, Q. J. Roy. Meteorol. Soc., 89, 339–348,

1963.
Tobin, C. D., Revercomb, H. E., Knuteson, R. O., Lesht, B. M., Strow, L. L., Hannon, S. E., Feltz, W. F., Moy, L. A., Fetzer, E. J., and Cress, T. S.: ARM site atmospheric state best estimates for AIRS temperature and water vapor retrieval validation, J. Geophys. Res., 111, D09S14, doi:10.1029/ 2005JD006103, 2006.
Wendisch, M., Pilewskie, P., Pommier, J., Howard, S., Yang, P., Heymsfield, A. J., Schmitt, C. G., Baumgardner, D., and Mayer, B.: Impact of cirrus crystal shape on solar spectral irradiance: a case study for subtropical cirrus, J. Geophys. Res., 110, D03202, doi:10.1029/2004JD005294, 2005.
Wielicki, B. A., Barkstrom, B. R., Harrison, E. F., Lee, R. B., Smith, G. L., and Cooper, J. E.: Clouds and the earth's radiant energy system (CERES): an earth observing system experiment, B. Am. Meteorol. Soc., 77, 853–868, 1995.
Wielicki, B. A., Barkstrom, B. R., Baum, B. A., Charlock, T. P. et al.: Clouds and the earth's radiant energy system (CERES): algorithm overview, IEEE T. Geosci. Remote, 36, 1127–1141, 1998.
Winker, D.: Accounting for multiple scattering in retrievals from space lidar, 12th International Workshop on Lidar Multiple Scattering Experiments, International Society for Optical Engineering (SPIE) Proceedings, 5059, 128–139, 2003.
Winker, D. M., Vaughan, M. A., Omar, A. H., Hu, Y., Powell, K. A., Liu, Z., Hunt, W. H., and Young, S. A.: Overview of the CALIPSO mission and CALIOP data processing algorithms, J. Atmos. Ocean. Tech., 26, 2310–2323, doi:10.1175/2009JTECHA1281.1, 2009.
Wylie, D. P. and Menzel, W. P.: Eight years of high cloud statistics using HIRS, J. Climate, 12, 170–184, 1999.
Young, S. A. and Vaughan, M. A.: The retrieval of profiles of particulate extinction from cloud aerosol lidar infrared pathfinder satellite observations (CALIPSO) data: algorithm description, J. Atmos. Ocean. Tech., 26, 1105–1119, doi:10.1175/2008JTECHA1221.1, 2009.

Table 1. Latitude, longitude, instruments, period of measurements for each sites.

Sites	SIRTA	SGP	TWP	NSA
Latitude/Longitude	48°42′ N/2°12′ E	36°36′ N/−97°29′ E	−0°31′ N/166°5′ E	71°18′ N/−156°39′ E
Altitude a.s.l.	156 m	318 m	7 m	20 m
Period of measurement	2002–2007	1998–2003	2003	2003–2005
Instruments				
Water vapor	GPS	Microwave radiometer		
Aerosol		Sun-photometer		
Radiative fluxes		BSRN station		
Cloud	LNA lidar	Raman lidar	Micropulse lidar	

ACPD
9, 26777–26832, 2009

Table 2. Seasonal and annual averages of integrated water vapor (IWV in cm) and aerosol optical thickness (AOT) in the Table 2A, cirrus cloud base altitude (CBH in km) and optical thickness (COT) in the Table 2B at ARM SGP Lamont, ARM TWP Nauru, ARM NSA Barrow, and SIRTA Palaiseau sites.

Aerosol and water vapor variability					
TABLE 2A	Winter IWV/AOT	Spring IWV/AOT	Summer IWV/AOT	Autumn IWV/AOT	Annual IWV/AOT
ARM SGP, Lamont	1.1/0.06	2.0/0.14	3.8/0.15	2.3/0.09	2.3/0.11
SIRTA, Palaiseau	0.9/0.07	1.3/0.12	2.2/0.11	1.6/0.08	1.5/0.10
ARM TWP, Nauru	5.7/0.1	5.8/0.09	5.1/0.12	4.8/0.08	5.3/0.10
ARM NSA, Barrow	–/–	0.6/0.08	1.4/0.07	1.6/0.04	1.2/0.07

Cirrus cloud macrophysical and optical properties variability					
TABLE 2B	Winter CBH/COT	Spring CBH/COT	Summer CBH/COT	Autumn CBH/COT	Annual CBH/COT
ARM SGP, Lamont	9.3/0.17	9.5/0.19	10.9/0.18	10.0/0.15	9.9/0.17
SIRTA, Palaiseau	9.3/0.17	9.2/0.21	9.3/0.16	9.5/0.19	9.3/0.18
ARM TWP, Nauru	11.8/0.22	11.9/0.23	11.8/0.29	12.4/0.21	12.0/0.24
ARM NSA, Barrow	–/–	7.9/–	8.3/0.11	7.7/0.02	8.1/0.08

ACPD
9, 26777–26832, 2009

Table 3. Accuracy of shortwave clear-sky model for each site. Values correspond to the root mean square error (RMSE) and the standard error. Unit: $W\,m^{-2}$.

SW	SIRTA, Palaiseau	ARM SGP Lamont	ARM TWP Nauru	ARM NSA Barrow
RMSE	13.8	12.1	6.9	9.7
Std. Err.	3.9	2.1	2.8	2.3

ACPD
9, 26777–26832, 2009

Table 4. CRE_{SW} for each cirrus cloud class. Unit: $W\,m^{-2}$. Sampling for each class is mentioned in parentheses. Cirrus cloud classes yielding CRE values significantly different from clear-sky references are in bold.

Cirrus cloud COT classes		Cirrus cloud base altitude classes			
		Low (7 km<CBH<9 km)	Medium (9 km<CBH<11 km)	High (CBH>11 km)	Average
Subvisible (COT<0.03)	SIRTA	0.3 (36)	6.6 (66)	−1.4 (249)	−0.8 (424)
	SGP	7.2 (19)	0.4 (35)	**−3.6** (50)	−0.3 (104)
	TWP	4.4 (81)	0.7 (92)	−0.5 (58)	2.2 (307)
	NSA	2.0 (19)	**−3.3** (32)	6.1 (3)	1.6 (73)
Semi-transparent (0.03<COT<0.3)	SIRTA	**−20.8** (79)	**−11.1** (244)	**−15.1** (470)	**−12.4** (974)
	SGP	**−16.3** (74)	**−14.7** (112)	**−12.8** (54)	**−14.8** (240)
	TWP	**−7.3** (131)	**−12.0** (154)	**−7.3** (57)	**−12.3** (548)
	NSA	**−26.4** (44)	**−32.0** (40)	**−13.2** (2)	**−24.9** (123)
Thick (COT>0.3)	SIRTA	**−148.1** (82)	**−108.7** (176)	**−71.5** (145)	**−95.4** (501)
	SGP	**−96.9** (94)	**−97.1** (89)	**−118.2** (12)	**−98.2** (195)
	TWP	**−83.5** (134)	**−76.3** (80)	**−63.9** (19)	**−96.1** (398)
	NSA	**−88.1** (29)	**−105.1** (6)	/	**−94.6** (44)
Average	SIRTA	**−58.2** (201)	**−45.4** (501))	**−18.7** (900)	**−31.9** (1602)
	SGP	**−52.7** (200)	**−42.8** (256)	**−17.8** (127)	**−40.9** (583)
	TWP	**−33.8** (370)	**−19.1** (351)	**−11.5** (141)	**−24.0** (862)
	NSA	**−39.6** (94)	**−24.7** (83)	**−3.8** (6)	**−31.7** (183)

ACPD
9, 26777–26832, 2009

Table 5. Contingency table of measured and calculated CRE_{SW} for all data sets. Unit: $W\,m^{-2}$ and percentage of cases for each range of measured CRE_{SW}.

CRE_{SW}		Measured			
Calculated	Percentage	0 to −10	−10 to −20	−20 to −50	<−50
0 to −10	19.2	**13.9**	3.7	8.0	1.8
−10 to −20	17.3	2.5	**10.8**	6.9	2.7
−20 to −50	27.3	2.1	2.2	**9.7**	10.8
<−50	36.2	0.6	0.7	2.6	**21.0**

ACPD

9, 26777–26832, 2009

Table 6. Accuracy of longwave clear-sky model for each site. Values correspond to the root mean square error (RMSE) and the standard error. Unit: $W\,m^{-2}$.

LW	SIRTA, Palaiseau	ARM SGP Lamont	ARM TWP Nauru	ARM NSA Barrow
RMS	5.1	5.9	4.9	6.8
Std. Err.	1.4	1.8	1.8	2.8

Table 7. CRE_{LW} for each cirrus cloud class. Unit: $W\,m^{-2}$. Sampling for each class is mentioned in parentheses. Cirrus cloud classes yielding CRE values significantly different from clear-sky references are in bold.

Cirrus cloud COT classes		Cirrus cloud base altitude classes			
		Low (7 km<CBH<9 km)	Medium (9 km<CBH<11 km)	High (CBH>11 km)	Average
Subvisible (COT<0.03)	SIRTA	**2.1** (36)	**2.0** (66)	1.1 (249)	**1.8** (424)
	SGP	**6.3** (19)	**7.0** (35)	**2.5** (50)	**4.7** (104)
	TWP	1.0 (81)	0.3 (92)	0.2 (58)	0.9 (307)
	NSA	2.0 (19)	0.8 (32)	0.5 (3)	2.1 (73)
Semi-transparent (0.03<COT<0.3)	SIRTA	**7.3** (79)	**6.7** (244)	**2.6** (470)	**5.3** (974)
	SGP	**8.1** (74)	**8.9** (112)	**6.7** (54)	**8.2** (240)
	TWP	0.6 (131)	0.3 (154)	0.2 (57)	**2.1** (548)
	NSA	**9.2** (44)	1.6 (40)	−1.2 (2)	**6.0** (123)
Thick (COT>0.3)	TWP	**26.9** (82)	**15.3** (176)	**5.0** (145)	**15.2** (501)
	SGP	**13.1** (94)	**12.3** (89)	**7.5** (12)	**12.4** (195)
	TWP	**2.8** (134)	0.5 (80)	0.6 (19)	**3.3** (398)
	NSA	**12.4** (29)	0.2 (6)	/	**10.9** (44)
Average	SIRTA	**14.3** (201)	**9.1** (501)	**2.5** (900)	**6.0** (1602)
	SGP	**10.4** (200)	**9.7** (256)	**5.2** (127)	**9.0** (583)
	TWP	1.4 (370)	0.3 (351)	0.6 (141)	0.8 (862)
	NSA	**8.7** (94)	1.4 (83)	−0.4 (6)	**5.1** (183)

ACPD
9, 26777–26832, 2009

Table 8. Contingency table of measured and calculated CRE_{LW} for all data sets. Unit: $W\,m^{-2}$ and percentage of cases for each range of measured CRE_{LW}.

CRE_{LW}		Measured			
Calculated	Percentage	0 to 5	5 to 10	10 to 20	>20
0 to 5	39.8	**25.3**	8.3	4.3	1.2
5 to 10	29.8	8.9	**16.6**	7.0	2.9
10 to 20	21.1	1.3	2.3	**8.8**	4.0
>20	9.2	0.0	0.2	0.1	**0.8**

ACPD
9, 26777–26832, 2009

Table 9. Seasonal and annual averages of SW/LW/NET instantaneous cirrus cloud radiative forcing at ARM SGP, ARM TWP, and SIRTA sites. Units: $W\,m^{-2}$.

	Winter SW/LW/NET	Spring SW/LW/NET	Summer SW/LW/NET	Autumn SW/LW/NET	Annual SW/LW/NET
ARM SGP, Lamont	−25.3/18.3/−7.0	−37.1/16.2/−20.9	−39.5/10.7/−28.8	−30.2/15.9/−14.3	−33.1/15.1/−18.0
ARM TWP, Nauru	−49.4/1.0/−48.4	−38.7/1.3/−37.5	−29.8/0.9/−28.7	−16.2/0.8/−15.4	−33.0/1.0/−32.0
SIRTA, Palaiseau	−15.6/8.0/−7.6	−31.3/9.6/−21.7	−25.6/7.8/−16.8	−15.4/7.0/−8.4	−23.6/8.1/−15.5

Table 10. Seasonal and annual averages of SW/LW/NET cumulative cirrus cloud radiative forcing at ARM SGP, ARM TWP, and SIRTA sites. Units: $W\,m^{-2}$.

	Winter SW/LW/NET	Spring SW/LW/NET	Summer SW/LW/NET	Autumn SW/LW/NET	Annual SW/LW/NET
ARM SGP, Lamont	−2.3/5.1/2.8	−6.2/5.6/−0.6	−7.6/3.5/−4.1	−4.4/4.4/0.0	−5.1/4.6/−0.5
ARM TWP, Nauru	−17.1/0.7/−16.4	−12.8/0.8/−12.0	−9.3/0.6/−8.7	−5.4/0.5/−4.9	−10.6/0.7/−9.9
SIRTA, Palaiseau	−5.1/6.9/1.8	−12.6/7.0/−5.6	−9.0/4.6/−4.3	−3.8/4.2/0.4	−7.6/5.6/−2.0

ACPD
9, 26777–26832, 2009

Table 11. Seasonal and annual averages of SW/LW/NET instantaneous cirrus cloud radiative forcing. Each value corresponds to 75° S to 45° S zone, 45° S to 15° S zone, 15° S to 15° N zone, 15° N to 45° N zone, and 45° N to 75° N zone. Units: $W\,m^{-2}$.

	75° S/45° S SW/LW/NET	45° S/15° S SW/LW/NET	15° S/15° N SW/LW/NET	15° N/45° N SW/LW/NET	45° N/75° N SW/LW/NET
Winter	−11.0/6.8/−4.2	−20.8/10.1/−10.7	−20.4/9.9/−10.5	−9.9/10.8/0.9	−8.8/8.4/−0.4
Spring	−10.5/7.5/−3.0	−20.4/11.2/−9.2	−20.8/10.1/−10.7	−17.9/10.1/−7.8	−8.4/4.7/−3.7
Summer	−12.1/7.1/−2.9	−17.5/8.3/−9.2	−21.8/6.3/−15.5	−20.9/7.2/−13.7	−13.0/7.8/−5.2
Autumn	−15.8/7.5/−8.3	−19.9/10.2/−9.7	−18.7/9.6/−9.1	−14.0/10.9/−3.1	−6.1/9.7/3.6
Annual	−13.3/7.2/−4.5	−19.7/10.0/−9.7	−20.4/9.0/−11.5	−15.7/9.8/−5.9	−9.0/7.2/−1.8

ACPD
9, 26777–26832, 2009

Table 12. Seasonal and annual averages of SW/LW/NET cumulative cirrus cloud radiative forcing. Each value corresponds to 75° S to 45° S zone, 45° S to 15° S zone, 15° S to 15° N zone, 15° N to 45° N zone, and 45° N to 75° N zone. Units: $W\,m^{-2}$.

	75° S/45° S SW/LW/NET	45° S/15° S SW/LW/NET	15° S/15° N SW/LW/NET	15° N/45° N SW/LW/NET	45° N/75° N SW/LW/NET
Winter	−1.8/0.8/1.0	−4.1/1.8/−2.3	−5.5/2.8/−2.7	−1.3/1.6/0.3	−0.4/0.8/0.4
Spring	−1.2/0.8/−0.4	−2.9/1.7/−1.2	−5.4/2.7/−2.7	−3.4/1.7/−1.7	−1.6/0.7/−0.9
Summer	−1.2/1.2/0	−2.0/1.0/−1.0	−5.3/1.5/−3.8	−4.8/1.4/−3.4	−3.1/1.4/−1.6
Autumn	−2.6/1.0/−1.6	−2.9/1.4/−1.5	−4.6/2.5/−2.1	−2.3/1.9/−0.4	−0.8/1.3/0.5
Annual	−1.8/0.9/−0.8	−3.0/1.5/−1.5	−5.2/2.4/−2.8	−2.9/1.6/−1.3	−1.3/0.9/−0.4

ACPD
9, 26777–26832, 2009

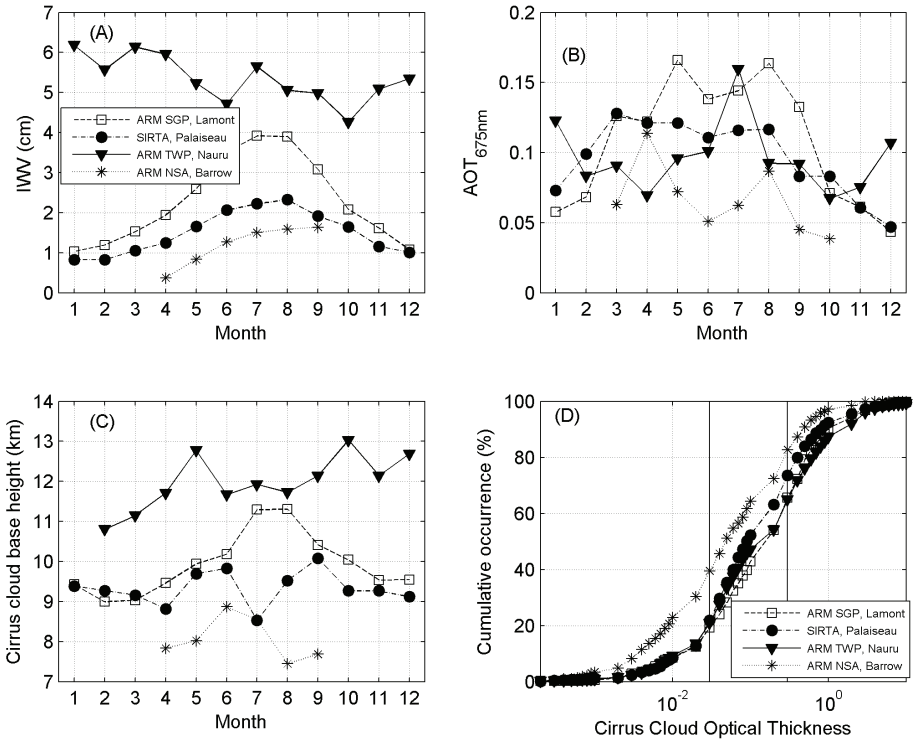

Fig. 1. Monthly mean integrated water vapor **(A)**, aerosol optical thickness **(B)** and cirrus cloud base altitude **(C)** for each site. **(D)** is the cumulative distribution of the cirrus cloud optical thickness. Black triangles correspond to ARM TWP Nauru site, white squares to ARM SGP Lamont site, black dots to SIRTA Palaiseau site, and black stars to ARM NSA Barrow site.

ACPD
9, 26777–26832, 2009

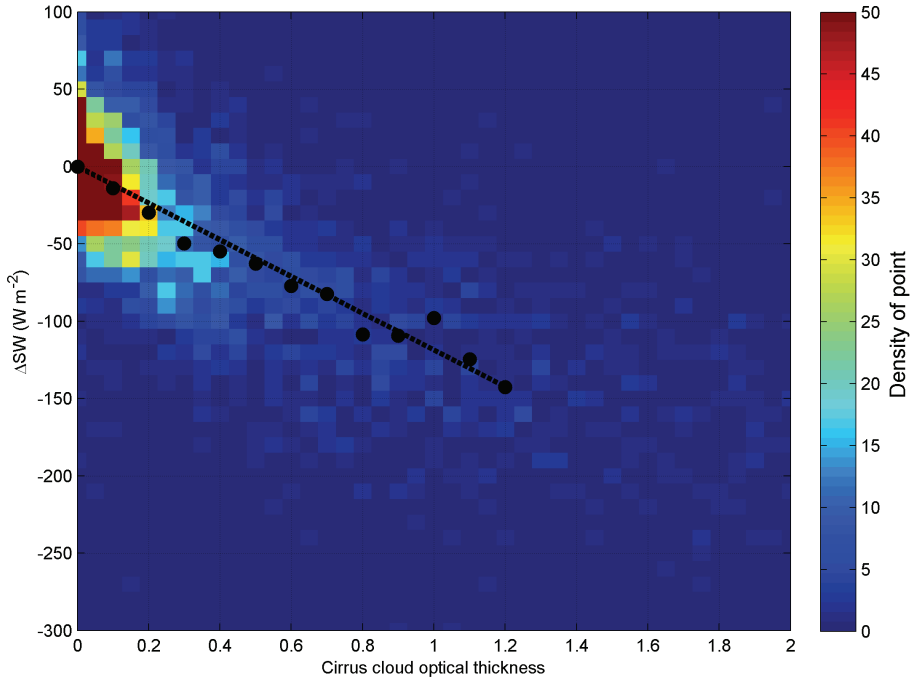

Fig. 2. Scatter plot of the shortwave cirrus cloud effect (CRE_{SW}) versus COT for the data collected in all the sites. The dashed line is the best linear fit optimized by the method of the least squares applied on the CRE_{SW} median every 0.1COT step. The dot markers correspond to the CRE_{SW} median every 0.1COT step.

ACPD

9, 26777–26832, 2009

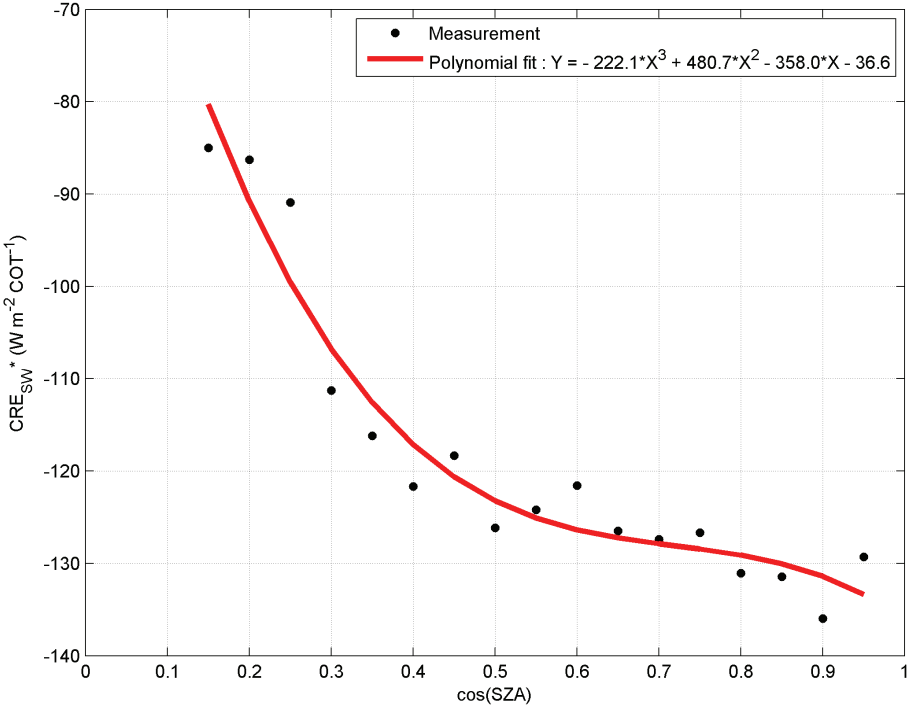

Fig. 3. Scatter plot of the sensitivity of CRE_{SW} to COT ($CRE_{SW}*$) versus the cosine of the solar zenith angle (cos(SZA)) for the data collected at all the sites. The red line is the best polynomial fit optimized by the method of the least squares applied on the $CRE_{SW}*$ median every 0.05cos(SZA) step. The black dot markers correspond to the $CRE_{SW}*$ median every 0.05cos(SZA) step.

ACPD
9, 26777–26832, 2009

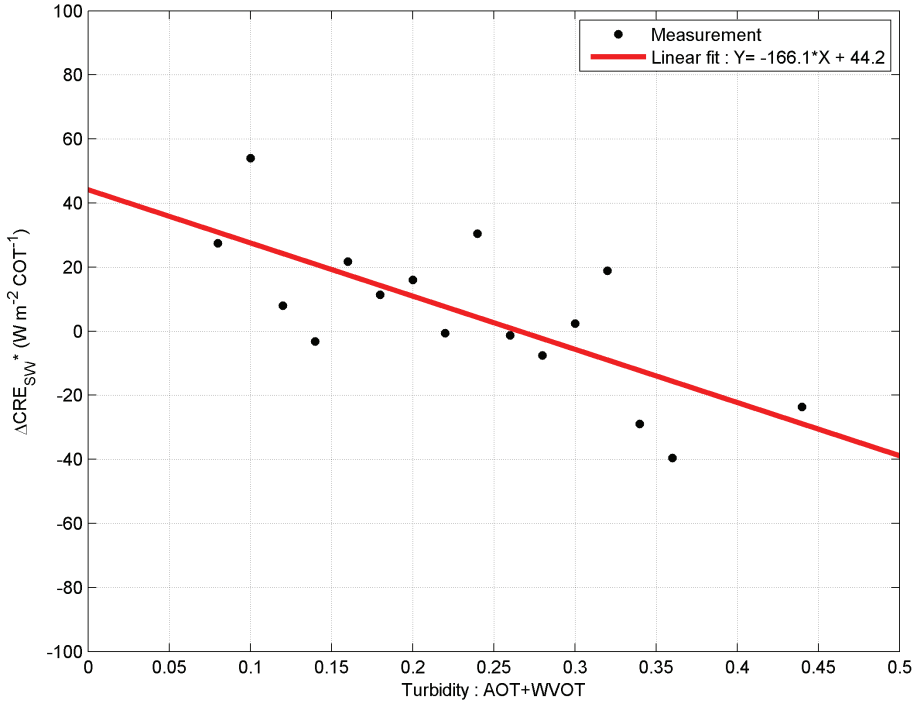

Fig. 4. Scatter plot of the sensitivity of $CRE_{SW}*$ residual ($\Delta CRE_{SW}*$) previously adjusted with cos(SZA) versus the turbidity represented for this study by AOT+WVOT. The red line is the best linear fit optimized by the method of the least squares applied on the $\Delta CRE_{SW}*$ median every 0.02AOT+WVOT step. The black dot markers correspond to the $\Delta CRE_{SW}*$ median every 0.02AOT+WVOT step.

ACPD
9, 26777–26832, 2009

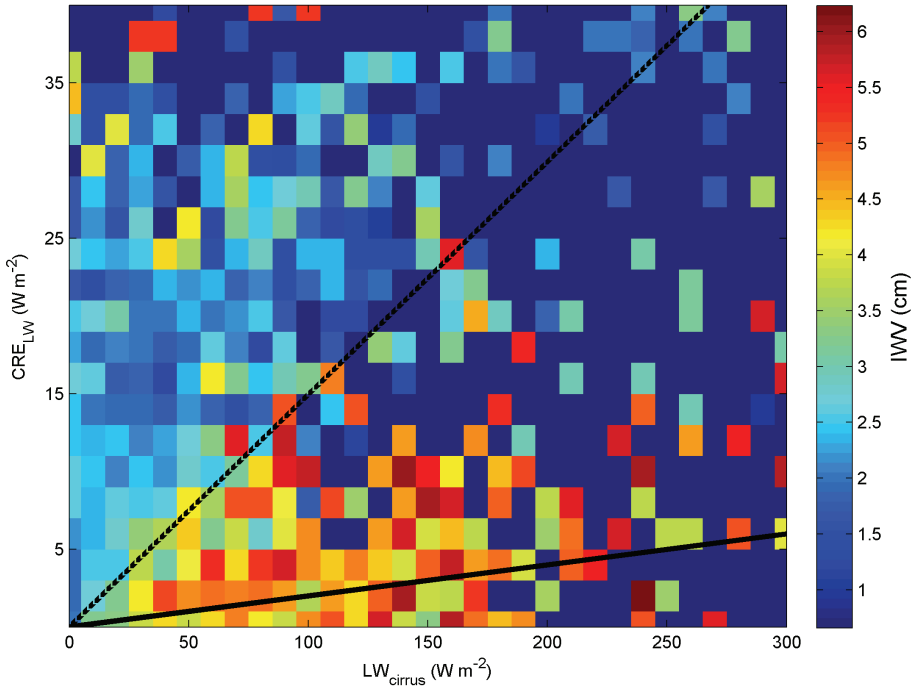

Fig. 5. Scatter plot of the longwave cirrus cloud effect (CRE_{LW}) versus cirrus cloud emissive power for the data collected at all the sites. Colored area represents the integrated water vapor content: red for very wet atmosphere and blue for very dry atmosphere. Black line corresponds to best linear fit adjusted to 50% wettest atmosphere and dashed black line to 50% driest atmosphere.

ACPD

9, 26777–26832, 2009

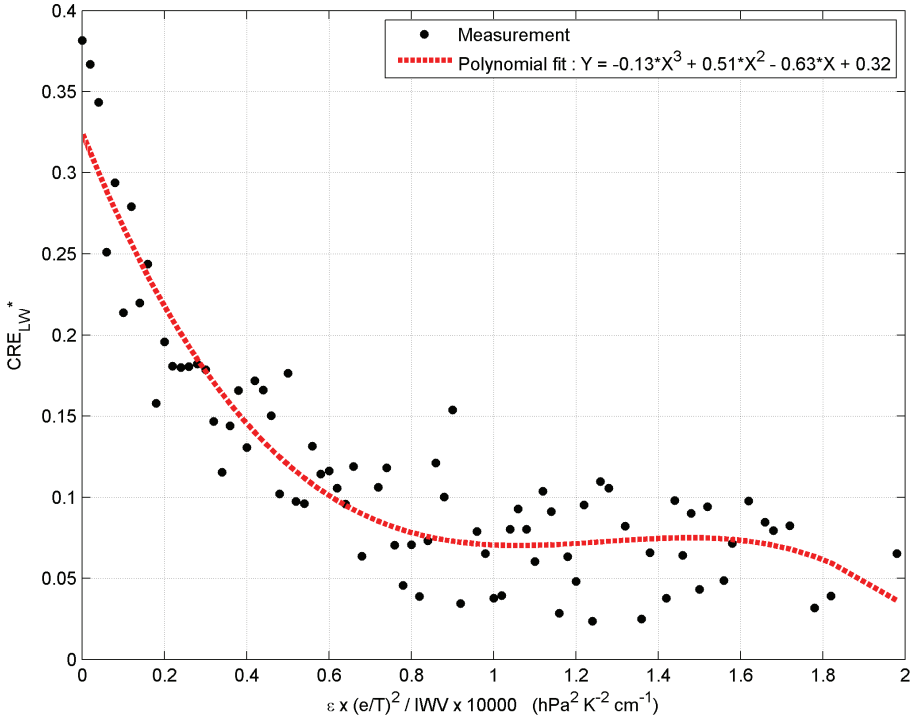

Fig. 6. Scatter plot of the sensitivity of $CRE_{LW}*$ versus γ parameter. The red line is the best polynomial fit optimized by the method of the least squares applied to the $CRE_{LW}*$ median every 0.02γ step. The black dot markers correspond to the $CRE_{LW}*$ median every 0.02γ step.

ACPD
9, 26777–26832, 2009

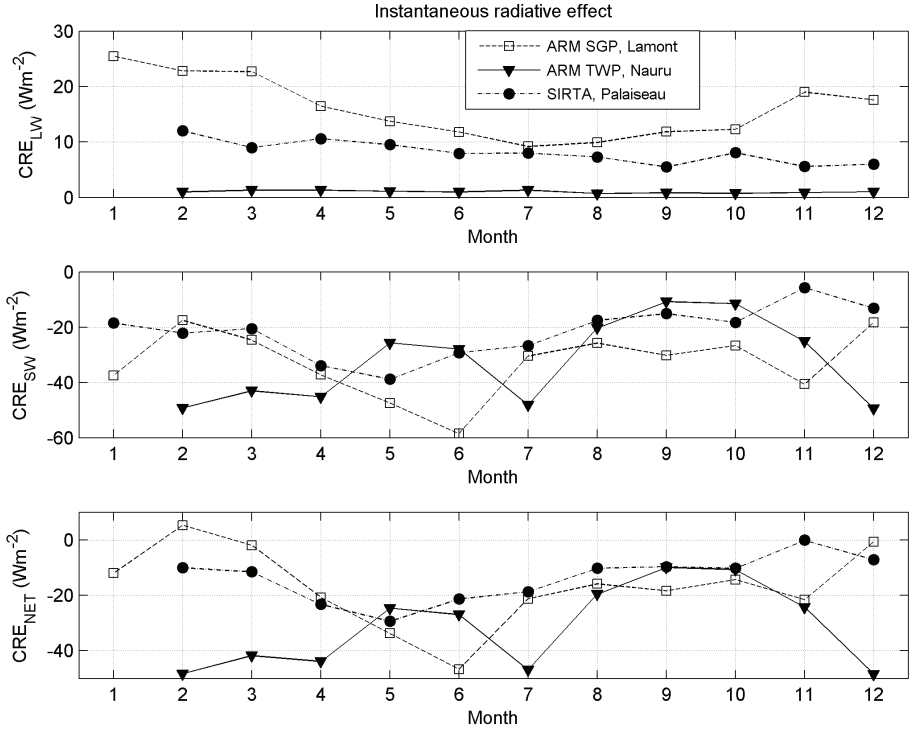

Fig. 7. Monthly mean instantaneous cirrus cloud radiative effect on longwave, shortwave, and net fluxes over ARM SGP, ARM TWP, and SIRTA sites.

ACPD
9, 26777–26832, 2009

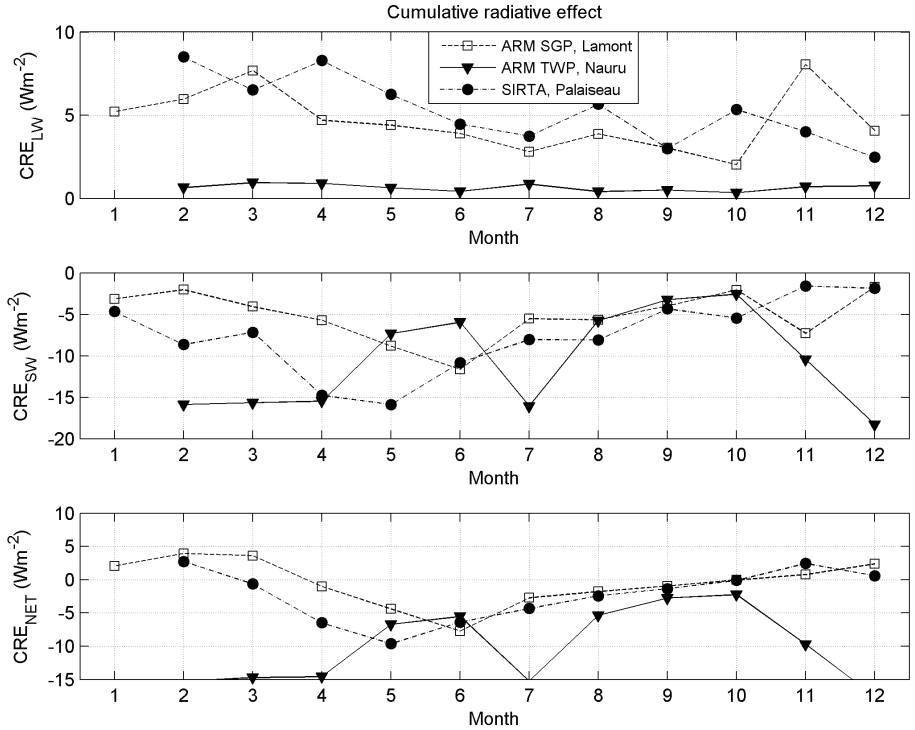

Fig. 8. Monthly mean cumulative cirrus cloud radiative effect on longwave, shortwave and net fluxes over ARM SGP, ARM TWP, and SIRTA sites.

ACPD
9, 26777–26832, 2009

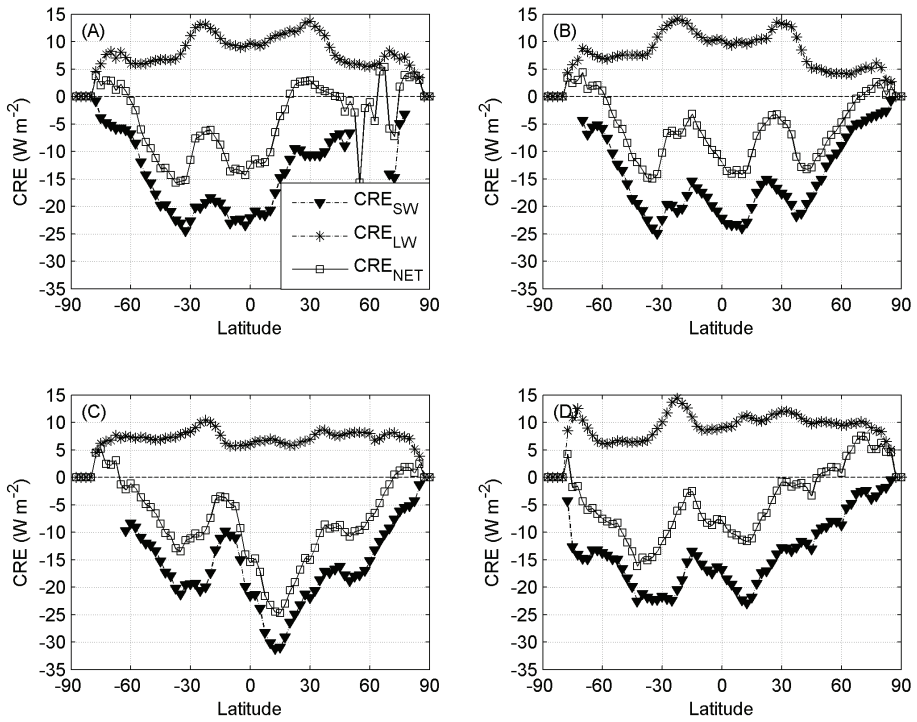

Fig. 9. Zonal cirrus cloud instantaneous effect at the surface for the different seasons: **(A)** winter, **(B)** spring, **(C)** summer and **(D)** autumn. Black triangles correspond to shortwave cirrus cloud radiative effect, stars to the longwave radiative effect, and squares to the net radiative effect at the surface.

ACPD
9, 26777–26832, 2009

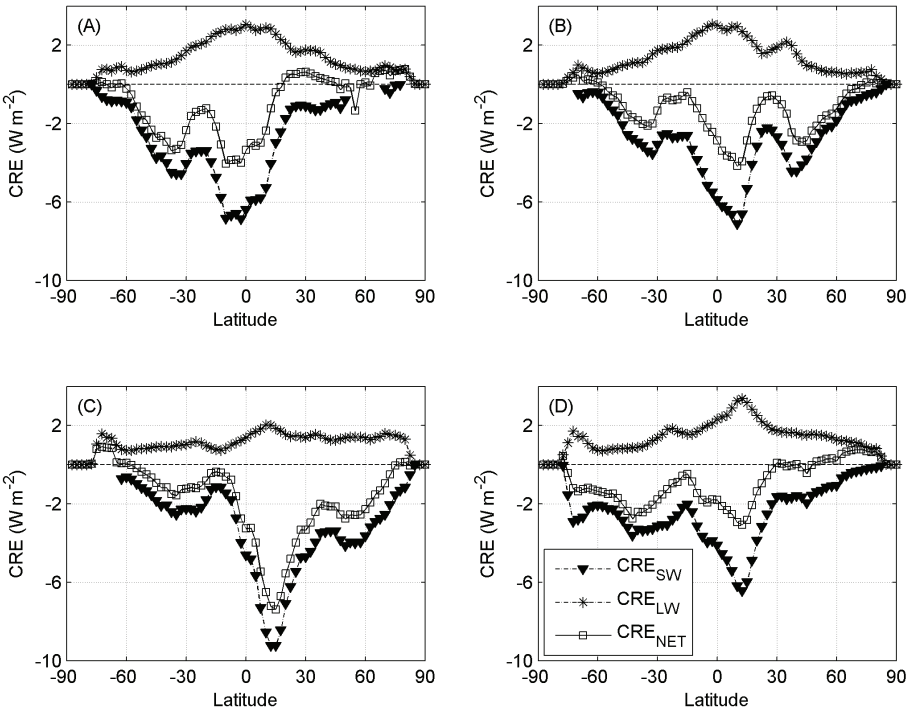

Fig. 10. Zonal cirrus cloud cumulative effect at the surface for the different seasons: **(A)** winter, **(B)** spring, **(C)** summer and **(D)** autumn. Black triangles correspond to shortwave cirrus cloud radiative effect, stars to the longwave radiative effect, and squares to the net radiative effect at the surface.

ACPD
9, 26777–26832, 2009